



Retrieving the global distribution of threshold of wind erosion from satellite data and
implementing it into the GFDL AM4.0/LM4.0 model

Bing Pu^{1,2,*}, Paul Ginoux², Huan Guo^{2,3}, N. Christine Hsu⁴, John Kimball⁵, Beatrice
Marticorena⁶, Sergey Malyshev², Vaishali Naik², Norman T. O'Neill⁷, Carlos Pérez
García-Pando⁸, Joseph M. Prospero⁹, Elena Shevliakova², Ming Zhao²

¹Atmospheric and Oceanic Sciences Program, Princeton University,
Princeton, New Jersey 08544

²NOAA Geophysical Fluid Dynamics Laboratory, Princeton, New Jersey 08540

³Cooperative Programs for the Advancement of Earth System Science, University
Corporation for Atmospheric Research, Boulder, Colorado, 80301

⁴NASA Goddard Space Flight Center, Greenbelt, Maryland, 20771

⁵Department of Ecosystem and Conservation Sciences, University of Montana,
Missoula, Montana 59812

⁶LISA, Universités Paris Est-Paris Diderot-Paris

⁷Département de géomatique appliquée, Université de Sherbrooke

⁸Barcelona Supercomputing Center, Barcelona, Spain, 08034

⁹Rosenstiel School of Marine and Atmospheric Sciences, University of Miami, Miami,
Florida, 33149

* Current affiliation: Department of Geographical and Atmospheric Science, the
University of Kansas, Lawrence, Kansas, 66045



1 **Abstract.** Dust emission is initiated when surface wind velocities exceed the threshold
2 of wind erosion. Most dust models used constant threshold values globally. Here we use
3 satellite products to characterize the frequency of dust events and surface properties. By
4 matching this frequency derived from Moderate Resolution Imaging Spectroradiometer
5 (MODIS) Deep Blue aerosol products with surface winds, we are able to retrieve a
6 climatological monthly global distribution of wind erosion threshold ($V_{threshold}$) over dry
7 and sparsely-vegetated surface. This monthly two-dimensional threshold velocity is then
8 implemented into the Geophysical Fluid Dynamics Laboratory coupled land-atmosphere
9 model (AM4.0/LM4.0). It is found that the climatology of dust optical depth (DOD) and
10 total aerosol optical depth, surface PM₁₀ dust concentrations, and seasonal cycle of DOD
11 are better captured over the “dust belt” (i.e. North Africa and the Middle East) by
12 simulations with the new wind erosion threshold than those using the default globally
13 constant threshold. The most significant improvement is the frequency distribution of
14 dust events, which is generally ignored in model evaluation. By using monthly rather
15 than annual mean $V_{threshold}$, all comparisons with observations are further improved. The
16 monthly global threshold of wind erosion can be retrieved under different spatial
17 resolutions to match the resolution of dust models and thus can help improve the
18 simulations of dust climatology and seasonal cycle as well as dust forecasting.

19

20

21

22

23



24 **1. Introduction**

25 Mineral dust is one of the most abundant aerosols by mass and plays an important
26 role in the climate system. Dust particles absorb and scatter solar and terrestrial radiation,
27 thus modifying local energy budget and consequently atmospheric circulation patterns.
28 Studies have shown that the radiative effect of dust can affect a wide range of
29 environmental processes. Dust is shown to modulate West African (e.g., Miller and
30 Tegen, 1998; Miller et al., 2004; Mahowald et al., 2010; Strong et al., 2015) and Indian
31 (e.g., Jin et al., 2014; Vinoj et al., 2014; Jin et al., 2015; Jin et al., 2016; Solmon et al.,
32 2015; Kim et al., 2016; Sharma and Miller, 2017) monsoonal precipitation. During severe
33 droughts in North America, there is a positive feedback between dust and the
34 hydrological cycle (Cook et al., 2008, 2009; 2013). African dust is also found to affect
35 Atlantic tropical cyclone activities (e.g., Dunion and Velden, 2004; Wong and Dessler,
36 2005; Evan et al., 2006; Strong et al., 2018). When deposited on snow and ice, dust
37 reduces the surface reflectivity, enhancing net radiant energy loading and accelerating
38 snow and ice melting, and consequently affecting runoff (e.g., Painter et al., 2010; 2018;
39 Dumont et al., 2014). Dust can serve as ice nuclei and affect the formation, lifetime, and
40 characteristic of clouds (e.g., Levin et al., 1996; Rosenfield et al., 1997; Wurzler et al.,
41 2000; Nakajima et al., 2001; Bangert et al., 2012), perturbing the hydrological cycle. Iron
42 and phosphorus enriched dust is also an important nutrient for the marine and terrestrial
43 ecosystems and thus interacts with the ocean and land biogeochemical cycles (e.g., Fung
44 et al., 2000; Jickells et al., 2005; Shao et al., 2011; Bristow et al., 2010; Yu et al., 2015).

45 Given the importance of mineral dust, many climate models incorporate dust
46 emission schemes to simulate the life cycle of dust (e.g., Donner et al., 2011; Collins et



47 al., 2011; Watanabe et al., 2011; Bentsen et al., 2013). Mineral dust particles are lifted
48 from dry and bare soils into the atmosphere by saltation and sandblasting. This process is
49 initiated when surface winds reach a threshold velocity of wind erosion. The value of this
50 wind erosion threshold depends on soil and surface characteristics, including soil
51 moisture, soil texture and particle size, and presence of pebbles, rocks, and vegetation
52 residue (e.g., Gillette et al., 1980; Gillette and Passi, 1988; Raupach et al., 1993; Fécan et
53 al., 1999; Zender et al., 2003; Mahowald et al., 2005), and thus varies spatially and
54 temporally (Helgren and Prospero, 1987). Due to a lack of in-situ data at global scale and
55 uncertainties on these dependencies, most dust and climate models prescribe a spatially
56 and temporally constant threshold of wind erosion for simplicity. Globally uniform
57 values (e.g., around 6 to 6.5 m s⁻¹) are either directly used over dry surfaces (e.g., Tegen
58 and Fung, 1994; Takemura et al., 2000; Uno et al., 2001; Donner et al., 2011) or with
59 modulations related to other factors, such as soil moisture (e.g., Takemura et al., 2000;
60 Ginoux et al. 2001; Zender et al., 2003; Kok et al., 2014a). For instance, in the
61 Geophysical Fluid Dynamics Laboratory coupled land-atmosphere model AM4.0/LM4.0
62 (Zhao et al., 2018a, b), a constant threshold of 6 m s⁻¹ is used.

63 The threshold of wind erosion may be approximately inferred using observations.
64 For instance, Chomette et al. (1999) used the Infrared Difference Dust Index (IDDI) and
65 10 m winds reanalysis from the European Centre for Medium-Range Weather Forecasts
66 (ECMWF) between 1990 and 1992 to calculate the threshold of wind erosion over seven
67 sites over the Sahel and Sahara. The IDDI was used to determine whether there was a
68 dust event for subsequently calculating an emission index defined as the number of dust
69 events to the total number of potential events. The distribution of surface wind speed was



70 matched with the emission index, and the threshold of wind erosion was determined
71 when the emission index was around 0.9. The resulting average threshold of wind erosion
72 ranged from 6.63 m s^{-1} at a Sahelian site to about 9.08 m s^{-1} at a Niger site, consistent
73 with the model results by Marticorena et al. (1997).

74 Later, Kurosaki and Mikami (2007) used World Meteorological Organization
75 (WMO) station data from March 1998 to June 2005 to examine the threshold wind speed
76 in East Asia. Using the distribution of surface wind speed and associated weather
77 conditions (i.e., with or without dust emission events), they approximated a dust emission
78 frequency by dividing number of dust events to the total number of observations for each
79 wind bin, and then determined threshold wind speeds at the 5% and 50% levels,
80 corresponding to the most favorable and normal land surface conditions for dust
81 emission, respectively. They found that the derived threshold wind speed varied in space
82 and time, with a larger seasonal cycle in grassland regions, such as northern Mongolia,
83 and smaller seasonal variations in desert regions, such as the Taklimakan and Gobi
84 Deserts and the Loess Plateau. Cowie et al. (2014) applied a similar method over
85 northern Africa, using wind data observed between 1984 and 2012, and focused on
86 threshold winds at the 25%, 50%, and 75% levels.

87 Draxler et al. (2010) derived the distribution of threshold of wind erosion over the
88 U.S. by matching the frequency of occurrence (FoO) of Moderate Resolution Imaging
89 Spectroradiometer (MODIS) Deep Blue (Hsu et al., 2004) aerosol optical depth (AOD)
90 above 0.75 with the FoO of friction velocities extracted from the North American
91 Mesoscale (NAM) forecast model at each grid point. This new threshold and a soil
92 characteristics factor was then incorporated into the Hybrid Single-Particle Lagrangian



93 Integrated Trajectory (HYSPPLIT) model (Draxier and Hess, 1998) to forecast dust
94 surface concentrations. It was found that major observed dust plume events in June and
95 July 2007 were successfully captured by the model. Later, Ginoux and Deroubaix (2017)
96 used FoO derived from the MODIS Deep Blue dust optical depth (DOD) record to
97 retrieve the wind erosion threshold over East Asia.

98 For individual dust events, the threshold of friction velocity can also be
99 determined by fitting a second-order Taylor series to dust saltation flux measurements
100 (Barchyn and Hugenholtz, 2011; Kok et al., 2014b).

101 Nonetheless, a global distribution of threshold of wind erosion based on
102 observation that may be implemented in climate models is still lacking. In this study, we
103 propose a method to retrieve monthly global threshold of wind erosion (hereafter,
104 $V_{threshold}$) for dry and sparsely-vegetated surface using high-resolution satellite products
105 and reanalysis datasets. This two-dimensional threshold is then implemented into the
106 Geophysical Fluid Dynamics Laboratory (GFDL) coupled land-atmosphere model,
107 AM4.0/LM4.0 (Zhao et al., 2018a, b). The benefits of using this threshold in simulating
108 present-day climatology and seasonal cycles of dust are analyzed by comparing the
109 model results with observations.

110 The data and method used to retrieve the threshold of wind erosion are detailed in
111 section 2. The distribution of the derived $V_{threshold}$ and its implication in the climate model
112 is presented in section 3. Section 4 discusses the uncertainties associated with this
113 method, and major conclusions are summarized in section 5.

114

115



116 **2. Data and Methodology**

117 **2.1 Data**

118 **2.1.1 Satellite products**

119 1) MODIS Aqua and Terra dust optical depth

120 DOD is column-integrated extinction by mineral particles. Here daily DOD is
121 retrieved from MODIS Deep Blue aerosol products (collection 6, level 2; Hsu et al.,
122 2013; Sayer et al., 2013): aerosol optical depth (AOD), single-scattering albedo, and the
123 Ångström exponent. All the daily variables are first interpolated to a 0.1° by 0.1° grid
124 using the algorithm described by Ginoux et al. (2010). We require that the single-
125 scattering albedo at 470 nm to be less than 1 for dust due to its absorption of solar
126 radiation. This separates dust from scattering aerosols, such as sea salt. Then a continuous
127 function relating the Ångström exponent, which is highly sensitive to particle size (Eck et
128 al., 1999), to fine-mode AOD established by Anderson et al. (2005; their Eq. 5) is used to
129 separate dust from fine particles. Details about the retrieval process and estimated errors
130 are summarized by Pu and Ginoux (2018b). High-resolution MODIS DOD products have
131 been used to identify and characterize dust sources (Ginoux et al., 2012; Baddock et al.,
132 2016) and examine the variations of dustiness in different regions (e.g., Pu and Ginoux,
133 2016, 2017, 2018b).

134 Following the recommendation from Baddock et al. (2016), who found the
135 dust sources are better detected using DOD with a low-quality flag (i.e., QA=1) than that
136 with a high-quality flag (i.e., QA=3) as retrieved aerosol products were poorly flagged
137 over dust source regions, we also use DOD with the flag of QA=1. Both daily DOD
138 retrieved from Aqua and Terra platforms are used by averaging the two when both



139 products are available or using either one when only one product is available. Since
140 Terra passes the equator from north to south around 10:30 am local time (LT) and Aqua
141 passes the Equator from south to north around 13:30 pm LT, an average of the two
142 combines the information from both morning and afternoon hours. This process also
143 largely reduces missing data (Pu and Ginoux, 2018b). This combined daily DOD,
144 hereafter MODIS DOD, is available from January 2003 to December 2015 at a resolution
145 of 0.1° by 0.1° grid.

146

147 2) Soil moisture

148 Soil moisture is an important factor that affects dust emission (Fécan et al., 1999).
149 Daily surface volumetric soil moisture (VSM) retrievals derived from similar calibrated
150 microwave (10.7 GHz) brightness temperature observations from the Advanced
151 Microwave Scanning Radiometer-Earth Observing System (AMSR-E) onboard the
152 NASA Aqua satellite (from June 2002 to October 2011) and the Advanced Microwave
153 Scanning Radiometer 2 (AMSR2) sensor onboard the JAXA GCOM-W1 satellite (from
154 July 2012 to June 2017) from the University of Montana (Du et al., 2017a; Du et al.,
155 2017b) was used. Both AMSR-E and AMSR2 sensors provide global measurements of
156 polarized microwave emissions at six channels, with ascending and descending orbits
157 crossing the equator at around 1:30 pm and 1:30 am LT, respectively. The VSM
158 retrievals are derived from an iterative retrieval algorithm that exploits the variable
159 sensitivity of different microwave frequencies and polarizations, and minimizes the
160 potential influence of atmosphere, vegetation, and surface water cover on the soil signal.
161 The VSM record represents surface (top ~2 cm) soil conditions and shows favorable



162 global accuracy and consistent performance (Du et al. 2017b), particularly over areas
163 with low to moderate vegetation cover that are also more susceptible to wind erosion.
164 The horizontal resolution of the product is about 25 km by 25 km, and the daily product
165 from January 2003 to December 2015 is used. The ascending and descending orbit VSM
166 retrievals are averaged to get the mean VSM for each day.

167

168 3) Snow cover

169 Snow cover may affect dust emission in the mid-latitudes during spring, for
170 instance, over northern China (Ginoux and Deroubaix, 2017). The interannual variation
171 of snow cover is also found to affect dust emission in regions, such as Mongolia
172 (Kurosaki and Mikami, 2004). Here monthly snow cover data from MODIS/Terra level
173 3 data (Hall and Riggs, 2015) with a resolution of 0.05° by 0.05° from 2003 to 2015 is
174 used. The high spatial resolution of the product is very suitable for this study.

175

176 4) Leaf area index (LAI)

177 Vegetation can protect soil from the effects of wind and thus modulate dust
178 emission (e.g., Marticorena and Bergametti, 1995; Zender et al., 2003). While dense
179 vegetation coverage can increase surface roughness and reduce near surface wind speed,
180 the roots of vegetation can increase soil cohesion and further reduce wind erosion. LAI
181 describes the coverage of vegetation with a unit of m^2/m^2 , i.e., leaf area per ground area.
182 Here monthly LAI retrieved by Boston University from MODIS onboard Aqua (via
183 personal communication with Ranga Myneni and Taejin Park; Boston University, 2016)
184 with a resolution of 0.1° by 0.1° from 2003 to 2015 is used.



185 **2.1.2 Reanalysis**

186 Surface wind speed is a critical factor that affects wind erosion. Here 6 hourly 10
187 m wind speed from the NCEP/NCAR reanalysis (Kalnay et al., 1996, hereafter NCEP1)
188 on a T62 Gaussian grid (i.e., 192 longitude grids equally spaced and 94 latitude grids
189 unequally spaced) is used. The NCEP1 is a global reanalysis with relatively long
190 temporal coverage, from 1948 to the present. We chose to use the NCEP1 reanalysis also
191 because surface winds in the GFDL AM4.0 model are nudged toward the NCEP1, and we
192 preferred to use the reanalysis surface wind that is closet to the model climatology.

193 ERA-Interim (Dee et al., 2011) is another global reanalysis produced from
194 ECMWF. It provides high spatial resolution (about 0.75° or 80 km) 6-hourly, daily, and
195 monthly reanalysis from 1979 to present day. Here we use soil temperature from the
196 ERA-Interim to determine the regions where wind erosion may be prohibited by the
197 frozen surface. Monthly temperature of the first soil layer (0 to 0.07 m) from 2003 to
198 2015 is used.

199

200 **2.1.3 Station data**

201 1) AERONET

202 The AERosol RObotic NETwork (AERONET; Holben et al., 1998) provides
203 quality assured cloud-screened (level 2) aerosol measurements from sunphotometer
204 records. In this paper we used the data products of the version 3.0 AERONET processing
205 routine. To examine model simulated DOD, we used coarse mode AOD (COD) at 500
206 nm processed by the Spectral Deconvolution Algorithm (O'Neill et al., 2003; hereafter
207 SDA). SDA COD monthly data is first screened to remove those months with less than



208 five days of records. To get the annual means, years with less than five months of records
209 were removed. Only stations with records of at least three years during the period were
210 used to calculate the 2003-2015 climatology (the same time period when MODIS DOD is
211 available). Overall, records from 313 stations were obtained.

212 AERONET monthly aerosol optical thickness (AOT) data around 550 nm (e.g.,
213 500 nm, 551 nm, 531 nm, 440 nm, 675 nm, 490 nm, 870 nm, etc.) and the Ångström
214 exponents across the dual wavelength of 440-675 nm, 440-870 nm, and 500-870 nm are
215 used to calculate AOD at 550 nm (τ_{550}). If AOT for 551 nm, 555 nm, 531 nm or 532 nm
216 exist, then these values are directly used as AOD 550 nm. Otherwise, the AOT at
217 wavelength λ_A (less than 550 nm), i.e., τ_A , AOT at wavelength λ_B (larger than 550 nm),
218 i.e., τ_B , and Ångström exponent between wavelengths λ_A and λ_B (α) are used to derive
219 AOD 550 nm using the following equations:

$$220 \quad \tau_{550} = \tau_A \left(\frac{550}{\lambda_A} \right)^{-\alpha} \quad \text{if } \tau_A \text{ is available,} \quad (1)$$

221

$$222 \quad \tau_{550} = \tau_B \left(\frac{550}{\lambda_B} \right)^{-\alpha} \quad \text{if } \tau_B \text{ is available.} \quad (2)$$

223

224 While this process of extrapolating to 550 nm using a classical Ångström exponent is a
225 bit incoherent with the higher order spectral approach of the SDA, errors due to the
226 choice of spectral order will be negligible in comparison with the types of model versus
227 measurement differences that we will be evaluating in this paper.

228 In a manner similar to the process of screening SDA COD data, monthly AOD
229 550 nm data with less than three days of records in a given month are removed. When
230 calculating the annual means we excluded years having less than five months of records.



231 Finally, to calculate the climatology of 2003-2015, only stations with at least three years
232 of records during this period are used totaling to 351.

233 We also developed a method to derive DOD at 550 nm from AOD 550 nm based
234 on the relationship between Ångström exponent and fine-mode AOD established by
235 Anderson et al. (2005; their Eq. 5). This adds a few more sites over the Sahel than the
236 SDA COD stations. DOD is calculated by subtracting the fine-mode AOD from the total
237 AOD. Due to the large uncertainties of single scattering albedo in AERONET records
238 over regions where AOD is lower than 0.4 (e.g., Dubovik and King, 2000; Holben et al.,
239 2006; Andrews et al., 2017), we did not use single scattering albedo to screen AOD to
240 further separate dust from scattering aerosols. Therefore, the derived AERONET DOD
241 over coastal stations may be contaminated by sea salt.

242

243 2) RSMAS surface dust concentration

244 The Rosenstiel School of Marine and Atmospheric Science (hereafter RSMAS
245 dataset) at University of Miami collected mass concentration of dust, sea salt, and sulfate
246 over stations globally, with most of stations on islands (Savoie and Prospero, 1989). The
247 dataset has been widely used for model evaluation (e.g., Ginoux et al., 2001; Huneus et
248 al., 2011).

249 Only stations with records longer than four years were used and of those stations
250 only those years with at least eight months of data are used for calculating climatological
251 annual means. So, totally 16 stations are used. Station names and locations are listed in
252 Table S1 of the Supplement. We compare the climatology of annual mean surface dust
253 concentration with model output during 2000-2015. Most station records end earlier than



254 1998. So here we also assume that the climatology of the surface dust concentrations do
255 not change greatly from the 1980s to the 2000s.

256

257 3) IMPROVE surface fine dust concentration

258 The Interagency Monitoring of Protected Visual Environments (IMPROVE)
259 network has collected near-surface particulate matter 2.5 (PM_{2.5}) samples in the U.S.
260 since 1988 (Malm et al., 1994; Hand et al., 2011). IMPROVE stations are located in
261 national parks and wilderness areas, and PM_{2.5} sampling is performed twice weekly
262 (Wednesday and Saturday; Malm et al., 1994) prior to 2000 and every third day
263 afterwards. Fine dust (with aerodynamic diameter less than 2.5 μm) concentration is
264 calculated using the concentrations of aluminum (Al), silicon (Si), calcium (Ca), iron
265 (Fe), and titanium (Ti) by assuming oxide norms associated with predominant soil
266 species (Malm et al., 1994; their Eq. 5). This dataset has been widely used to study
267 variations in surface fine dust in the U.S. (e.g., Hand et al., 2016; Hand et al., 2017, Tong
268 et al., 2017; Pu and Ginoux, 2018a). Here only monthly data with at least 50% of daily
269 data available in a month (i.e., at least 5 records) are used. Since station coverage over the
270 central U.S. increases after 2002 (e.g., Pu and Ginoux, 2018a), monthly station data from
271 2002 to 2015 are used and interpolated to a 0.5° by 0.5° grid using inverse distance
272 weighting interpolation. The gridded data are used to evaluate modeled surface fine dust
273 concentrations.

274

275 4) LISA PM₁₀ surface concentration



276 Surface PM₁₀ concentration from stations from the Sahelian Dust Transect, which
277 was deployed in 2006 under the framework of African Monsoon Multidisciplinary
278 Analysis International Program (Marticorena et al., 2010), were used to examine the
279 surface dust concentration over the Sahelian region. The data are maintained by
280 Laboratoire Interuniversitaire des Systèmes Atmosphériques (LISA) in the framework of
281 the International Network to study Deposition and Atmospheric composition in Africa
282 (INDAAF; Service National d'Observation de l'Institut National des Sciences de
283 l'Univers, France) network. Three stations are located within the pathway of Saharan and
284 Sahelian dust plumes moving towards the Atlantic Ocean. Here hourly PM₁₀
285 concentrations from these stations, Banizoumbou (Niger, 13.54° N, 2.66° E), Cinzana
286 (Mali, 13.28° N, 5.93° W), and M'Bour (Senegal, 14.39° N, 16.96° W), from 2006 to
287 2014 are used. The hourly station data are averaged to obtain daily and monthly mean
288 records to compare with model output.

289

290 **2.1.4 Other data**

291 Soil depth from the Food and Agriculture Organization of the United Nations
292 (FAO/IIASA/ISRIC/ISS-CAS/JRC, 2009) on a 0.08° by 0.08° resolution is used to
293 examine whether the soil depth is too shallow (i.e. less than 15 cm) for wind erosion.

294

295 **2.2 Retrieving threshold of wind erosion**

296 The monthly climatological threshold of wind erosion is retrieved by matching
297 the frequency distribution of the MODIS DOD at certain level with the frequency



298 distribution of surface 10 m winds from the NCEP1 reanalysis over the period from 2003
299 to 2015. The process can be summarized by the following steps:

300 Step1: Since dust is emitted from the dry and sparsely-vegetated surface, the daily DOD
301 data is first masked out to remove the influences of non-erodible factors and unfavorable
302 environmental conditions that are known to prevent dust emission using criteria as
303 follows: daily VSM less than $0.1 \text{ cm}^3 \text{ cm}^{-3}$; monthly LAI less than 0.3; monthly snow
304 cover less than 0.2%; monthly top-layer soil temperature higher than 273.15 K, i.e., over
305 unfrozen surface; and soil depth thicker than 15 cm.

306 Similar criteria have been used in previous studies to detect or confine dust source
307 regions. For instance, Kim et al. (2013) used NDVI less than 0.15, soil depth greater than
308 10 cm, surface temperature greater than 260 K, and without snow cover to mask
309 topography based dust source function. LAI less than 0.3 has been used as a threshold for
310 dust emission in the Community Land Model (Mahowald et al., 2010; Kok et al., 2014a),
311 while gravimetric soil moisture ranging from 1.01 to 11.2 kg kg^{-3} depending on soil clay
312 content is recommended to constrain dust emission (Fécan et al., 1999).

313 Step 2: Masked daily DOD from Step 1 is then interpolated to a 0.5° by 0.5° grid using
314 bilinear interpolation. This is close to the horizontal resolution of the GFDL
315 AM4.0/LM4.0 model used in this study. Then the cumulative frequency distribution of
316 daily DOD from 2003 to 2015 is derived at each grid point for each month.

317 Step 3: Daily maximum surface wind speed is first derived from 6-hourly NCEP1 surface
318 winds and then interpolated to a 0.5° by 0.5° grid. The cumulative frequency distribution
319 of daily maximum surface wind from 2003 to 2015 is then calculated at each grid point
320 for each month.



321 Step 4: A minimum value of DOD (DOD_{thresh}) is used to separate dust events from
322 background dust. The cumulative frequency (in %) of dust events passing this threshold
323 is compared to the cumulative frequency of surface winds. The minimum surface winds
324 with the same frequency correspond to the threshold of wind erosion, $V_{threshold}$ (see a
325 schematic diagram in Figure S1 in the Supplement). This operation is performed for all
326 grid points for each month. Ginoux et al. (2012) used $DOD_{thresh} = 0.2$ to quantify the FoO
327 of local dust events. Similarly, $DOD_{thresh} = 0.2$ is used here in major dusty regions (North
328 Africa, Middle East, India, northern China), while for less dusty regions, such as the U.S.,
329 South America, South Africa, and Australia, $DOD_{thresh} = 0.02$ is used. The reason to use a
330 lower DOD_{thresh} for less dusty regions is because: i) the overall dust emission in these
331 regions are at least ten times smaller than major dusty regions, such as North Africa (e.g.,
332 Huneus et al., 2011); ii) the frequency distribution of DOD in these regions also peaks at
333 a much lower DOD band (see discussion in section 3.3).

334 Figures 1a-e show the seasonal and annual mean FoO (days when DOD is greater
335 than DOD_{thresh}) using the DOD_{thresh} defined here. The shaded area covers major dust
336 sources, and the pattern is very similar to that obtained by Ginoux et al. (2012; their Fig.
337 5), although there are some differences, largely due to the masked DOD (i.e., from Step
338 1) used in this study and a lower threshold in less dusty regions.

339 Note that the selections of masking criteria in Step 1 and DOD_{thresh} in Step 4 are
340 empirical and can add uncertainties to this method. Also, we approximate dust emission
341 using cumulative frequency of DOD, which may overestimate dust emission in regions
342 where the contribution of transported dust is significant and thus underestimate the
343 $V_{threshold}$ in those regions.



344 2.3 Simulation design

345 The AM4.0/LM4.0 is a coupled land-atmosphere model newly developed at
346 GFDL (Zhao et al., 2018a,b). It uses the recent version of the GFDL Finite-Volume
347 Cubed-Sphere dynamical core (FV³; Putman and Lin, 2007), which is developed for
348 weather and climate applications with both hydrostatic and non-hydrostatic options.
349 Some substantial updates have been incorporated into the AM4.0, such as an updated
350 version of the model radiation transfer code, an alternate topographic gravity wave drag
351 formulation, a double-plume model representing shallow and deep convection, a “light”
352 chemistry mechanism, and modulation on aerosol wet removal by convection and frozen
353 precipitation (Zhao et al., 2018a,b). Here we used a model version with 33 vertical levels
354 (with model top at 1hPa) and cube-sphere with 192×192 grid boxes per cube face
355 (approximately 50 km grid size).

356 The aerosol physics is based in large part on that of the GFDL AM3.0 (Donner et
357 al., 2011), but with a simplified chemistry where ozone climatology from AM3.0
358 simulation (Naik et al., 2013) is prescribed. AM4.0 simulates the mass distribution of five
359 aerosols: sulfate, black carbon, organic carbon, dust, and sea salt. Dust is partitioned into
360 five size bins based on radius: 0.1~1 μm (bin 1), 1~2 μm (bin 2), 2~3 μm (bin 3), 3~6 μm
361 (bin 4), and 6~10 μm (bin 5). The dust emission scheme follows the parameterization of
362 Ginoux et al. (2001), as shown in the following equation:

$$363 \quad F_p = C \times S \times s_p \times V_{10m}^2 (V_{10m} - V_t) \quad (\text{if } V_{10m} > V_t), \quad (3)$$

364

365 where F_p is flux of dust of particle size class p , C is a scaling factor with a unit of $\mu\text{g s}^2$
366 m^{-5} , here C is set to 0.75×10^{-9} . S is the source function based on topographic depressions



367 (Ginoux et al., 2001), s_p is fraction of each size class, and V_{10m} is surface 10 m wind
368 speed, and $V_t = 6 \text{ m s}^{-1}$ is the threshold of wind erosion.

369 Three simulations with prescribed sea surface temperature (SST) and sea ice
370 (Table 2) were conducted from 1999 to 2015, with the first year discarded for spin up.
371 The Atmospheric Model Intercomparison Project (AMIP)-style SST and sea ice data
372 (Taylor et al., 2000) are from the Program for Climate Model Diagnosis and
373 Intercomparison (PCMDI), which combined HadISST (Rayner et al., 2003) from UK Met
374 Office before 1981 and NCEP Optimum Interpolation (OI) v2 SST (Reynolds et al.,
375 2002) afterwards. The surface winds in the simulations are nudged toward the NCEP1
376 reanalysis with a relaxation timescale of 6 hours (Moorthi and Suarez, 1992). Note that
377 the nudged surface winds are actually weaker than the surface wind speed simulated by
378 the standard version of AM4.0/LM4.0 without nudging, so the overall magnitude of dust
379 emission is lower than the standard version. Here we choose not to retune the dust
380 emission scheme but instead test the usage of $V_{threshold}$, which theoretically provides a
381 more physics-based way to improve dust simulation.

382 In the Control run, the default model setting is used for dust emission, with a
383 prescribed 6 m s^{-1} threshold of wind erosion (cf. Ginoux et al., 2019). In the $V_{thresh12mn}$
384 simulation, the observation based climatological monthly $V_{threshold}$ is used to replace the
385 constant wind erosion threshold. The default source function S in Eq. 3 only allows dust
386 emission over bare ground by masking out regions with vegetation cover. Since LAI
387 masking is already applied in the retrieval of $V_{threshold}$ (i.e., $LAI < 0.3$), we choose to use a
388 source function that is the same as the default source function S but without vegetation
389 masking, i.e., S' (Figure S2 in the supplement). This allows the influence of the spatial



390 and temporal variations of $V_{threshold}$ to be fully examined. The combination of source
391 function S' and $V_{threshold}$ also extends dust source from bare ground to sparsely vegetated
392 area as outlined by $V_{threshold}$, e.g., over central North America, central India, and part of
393 Australia, and can increase dust emission in these regions. The pattern of extended dust
394 source area largely resembles the vegetated dust source identified by Ginoux et al. (2012;
395 their Fig. 15b) and Kim et al. (2013; their Fig. 9). All the other settings are the same as
396 the Control run. The $V_{threshAnn}$ simulation is the same as the $V_{thresh12mn}$ but uses the
397 annual mean of $V_{threshold}$ for each month. Since the same SST and sea ice are prescribed
398 for all simulations, the differences in simulated dynamic vegetation by LM4.0 among the
399 three simulations are actually very small and can be ignored (see Figures S3-4 in the
400 Supplement).

401

402 3. Results

403 3.1 Threshold of wind erosion

404 Figures 1f-j show the derived threshold of wind erosion for each season and
405 annual mean. The seasonal variations of wind erosion are largely due to the variations of
406 land surface features examined here, such as soil moisture, soil temperature, snow cover,
407 and vegetation coverage in each month. $V_{threshold}$ is generally lower in MAM and JJA
408 (SON and DJF) for Northern (Southern) Hemisphere dusty regions than in other seasons.
409 $V_{threshold}$ values are also lower in major dust source regions (i.e., regions with a high FoO
410 in Figs. 1a-e). Globally, the lowest $V_{threshold}$ values ($\sim 3\text{-}5\text{ m s}^{-1}$) are located over North
411 Africa and the Middle East, while the highest values ($>10\text{ m s}^{-1}$) occur over northern
412 Eurasia.



413 Figure 2a shows the cumulative frequency of $V_{threshold}$ over the global land area for
414 each season and annual mean. The globally constant threshold 6 m s^{-1} used in the GFDL
415 AM4.0/LM4.0 is actually above the 50% level for all seasons and annual mean,
416 indicating the default setting in model likely overestimates the threshold of wind erosion.
417 In fact, the 50% level of $V_{threshold}$ is around 4.5 m s^{-1} for the annual mean and ranges from
418 4 m s^{-1} in JJA to about 5 m s^{-1} in SON and DJF.

419 The distributions of $V_{threshold}$ for annual mean (black bars) and dusty seasons
420 (color lines; MAM and JJA for the Northern Hemisphere and SON and DJF for the
421 Southern Hemisphere) for each dusty region (see Fig. 1f and Table 1 for locations) are
422 shown in Figs. 2b-j. In the Sahel, the annual mean $V_{threshold}$ peaks around 4 m s^{-1} (Fig. 2b).
423 This magnitude is lower than indicated from previous studies based on station
424 observations in the region, e.g., Helgren and Prospero (1987) found the threshold velocity
425 over eight stations in Northwest Africa ranged from 6.5 to 13 m s^{-1} during summer in
426 1974. Chomette et al. (1999) and Marsham et al. (2013) also reported higher wind
427 erosion thresholds around 6 - 9 m s^{-1} at individual stations. On the other hand, Cowie et al.
428 (2014) found that the annual threshold of wind erosion at the 25% level, i.e., when
429 surface condition is favorable for dust emission, can be lower than 6 m s^{-1} at some sites in
430 the Sahel (their Fig. 5). Several factors may contribute to the discrepancies. First, studies
431 suggest that reanalysis datasets may underestimate surface wind speed in spring and for
432 monsoon days in Africa (e.g., Largeron et al., 2015), and therefore could lead to a lower
433 value of $V_{threshold}$ than that derived from station observations. In fact, Bergametti et al.
434 (2017) found even 3-hourly wind speed record at stations may miss short events with
435 high wind speed. As mentioned earlier, using DOD frequency to approximate dust



436 emission may lead to an overestimation of dust emission over regions such as the
437 southern Sahel where transported dust is a large component and consequently an
438 underestimation of $V_{threshold}$. Different analysis time periods or methods to retrieve the
439 wind erosion threshold may also contribute to the differences.

440 The annual mean $V_{threshold}$ in the Sahara and Arabian Peninsula is a bit higher,
441 with mean values at 4.5 and 5.2 m s⁻¹, respectively (Figs. 2c-d). The $V_{threshold}$ over
442 northern China is even higher, with an annual mean of 7.9 m s⁻¹. This is consistent with
443 the results of Kurosaki and Mikami (2007), who found that under favorable land surface
444 conditions the threshold wind speed ranges from 4.4± 0.6 m s⁻¹ in Taklimakan Desert to
445 6.9± 1.2 m s⁻¹ over the Loess Plateau and around 9.8± 1.6 m s⁻¹ in the Gobi Desert. These
446 values are also consistent with Ginoux and Deroubaix (2017) who found that regional
447 mean wind erosion threshold over northern China ranges from 6.5 to 9.1 m s⁻¹. In India,
448 the $V_{threshold}$ peaks at about 4.5 m s⁻¹ and 6.5 m s⁻¹, respectively (Fig. 2f). The second peak
449 is probably related to anthropogenic dust sources over the central Indian subcontinent
450 (Ginoux et al., 2012). We also note that in the Northern Hemisphere, the $V_{threshold}$ in dusty
451 seasons is shifted towards lower values than the annual mean (blue and green lines in
452 Figs. 2b-g), but is similar to the annual mean in the Southern Hemisphere, indicating
453 stronger influences of surface variability in the Northern Hemisphere.

454

455 **3.2 $V_{threshold}$ in the GFDL AM4.0/LM4.0 model**

456 The derived $V_{threshold}$ is then implemented into the GFDL AM4.0/LM4.0 models.
457 In this section we analyze the model output using the default setting (Control), 12-month



458 ($V_{\text{thresh}12\text{mn}}$), and annual mean $V_{\text{threshold}}$ ($V_{\text{threshAnn}}$) to see how $V_{\text{threshold}}$ may affect the
459 simulation of DOD, surface dust concentration, and dust event frequency in the model.

460

461 **3.2.1 Climatology of AOD and DOD**

462 In order to compare the model results with observations, we first show the
463 climatology of AERONET AOD and COD from 2003 to 2015. As shown in Figure 3,
464 annual mean global AOD is highest over Africa, the Arabian Peninsula, Indian
465 subcontinent, and Southeast Asia. In the latter two regions, high sulfate concentrations
466 (e.g., Ginoux et al., 2006) and organic carbon from biomass burning in Southeast Asia
467 (e.g., Lin et al., 2014) contribute substantially to the total AOD. The SDA COD shows
468 the optical depth due to coarse aerosols, which includes both dust and sea salt, and sea
469 salt over coastal regions or islands can be a major contributor. Here, high values (>0.2)
470 are largely located over dusty regions such as North Africa, the Arabian Peninsula, and
471 northern India (Fig. 3b).

472 Figures 4a-b show the scatter plots of modeled AOD and COD in the Control run
473 versus AERONET AOD and COD, respectively. Here column-integrated extinction from
474 both dust and sea salt is used to calculate COD in the model. The relative differences
475 (%) between AM4.0 output and AERONET station data are also shown (Figs. 4c-d). The
476 percentage of DOD to total COD in the model is displayed at the bottom (Fig. 4e). The
477 simulated AOD is lower than that from the AERONET over North Africa, the Middle
478 East, and western India, largely due to low values of COD simulated in these regions
479 (Fig. 4d). Besides these regions, the COD over North America, South America, South
480 Africa, and northern Eurasia is also, for the most part, underestimated by the model. Dust



481 is the dominant contributor to the COD value over most of these low COD regions,
482 except over the central to eastern North America and central South America.

483 The underestimation of COD (and effectively DOD given its dominance in most
484 regions) was improved in the subsequent model run using a prescribed 12-month $V_{threshold}$.
485 Figure 5 shows the results from the $V_{thresh}12mn$ simulation. COD is better captured while
486 the AOD effectively moves from a negative to a slightly positive bias (Figs. 5a-d). Most
487 sites over North Africa and the Middle East show a relatively small difference with
488 AERONET COD (Fig. 5d). Over the Indian subcontinent, COD is overestimated, while
489 over North America excluding the east coast, northern Eurasia, and part of South
490 America, COD is also better captured than in the Control run.

491 These improvements are largely associated with a better simulation of DOD in the
492 “dust belt” (i.e., North Africa and the Middle East). Figure 6 shows the DOD at 550 nm
493 derived from AERONET AOD (see methodology for details) versus that from the
494 $V_{thresh}12mn$ simulation. Over most stations in the Sahel, Mediterranean coasts, and
495 central Middle East, the relative differences between modeled and observed DOD is
496 within $\pm 25\%$.

497 Figure 7 shows the regional averaged annual mean DOD over nine dusty regions
498 from MODIS and three simulations. The Control run largely underestimates DOD in all
499 regions, while the magnitude of DOD is better captured in the $V_{thresh}12mn$ and $V_{thresh}Ann$
500 simulations, although slightly overestimated in the Sahel and greatly overestimated over
501 Australia. In general, DOD simulated by the $V_{thresh}Ann$ run using a constant annual mean
502 $V_{threshold}$ is higher than that simulated by the $V_{thresh}12mn$ run, consistent with the higher
503 dust emission in the $V_{thresh}Ann$ run (Table S2 in the Supplement). Lack of soil moisture



504 constraint in the model, which is a very important element in capturing the variation of
505 DOD in Australia (Evans et al., 2016), may contribute to the large overestimation of
506 DOD in Australia.

507

508 **3.2.2 Climatology of surface dust concentration**

509 While DOD is a key parameter associated with the climate impact of dust, surface
510 dust concentration is an important factor affecting local air quality. Here we compare the
511 modeled surface dust concentration with RSMAS station observations. Model output is
512 averaged from 2000 to 2015 to form the annual climatology. Consistent with the DOD
513 output, the Control run largely underestimates surface dust concentrations at almost all of
514 the sites (except sites 9 and 15; Figure 8 top panel). The underestimation bias is reduced
515 in the $V_{\text{threshAnn}}$ simulation (Fig. 8, middle panel), with seven stations having
516 model/observation ratios between 0.5 and 2 (white triangles). Over the coastal U.S. (e.g.,
517 sites 16 and 13), dust concentrations are overestimated, consistent with the
518 overestimation of DOD over the U.S. and the Sahel (Fig. 7). Dust concentrations in
519 Australia and the east coast of China are also overestimated by more than five-folds.
520 Surface dust concentration is further improved in the $V_{\text{thresh12mn}}$ simulation (Fig. 8,
521 bottom), with eight stations showing a model/observation ratio between 0.5 and 2 and
522 only four stations overestimating or underestimating dust concentrations by more than
523 five times.

524 Simulated surface fine dust concentration (calculated as dust bin 1+0.25×dust bin
525 2) in the U.S. is compared with gridded IMPROVE data (Figure 9). While the Control
526 run largely underestimates surface fine dust concentration, the simulated concentration is



527 overall too high in the $V_{\text{threshAnn}}$ run. The spatial pattern of fine dust concentration is
528 better captured in the $V_{\text{thresh12mn}}$ run, with higher values over the southwestern U.S., but
529 the magnitude is still overestimated, and additional dust hot spots are simulated over the
530 northern Great plains and the Midwest, which are not shown in the IMPROVE data. Such
531 an overall overestimation may be attributed to lack of soil moisture modulation in the
532 dust emission scheme. The way in which dust bins are partitioned in the model can add
533 uncertainties to model's representation of surface fine dust concentrations as well. On
534 the other hand, the relatively low spatial coverage of IMPROVE sites over the northern
535 Great Plains and Midwest (e.g., Pu and Ginoux, 2018a) may also add uncertainties to the
536 data itself.

537

538 3.2.3 Seasonal cycles

539 Figure 10 compares the seasonal cycle of DOD from three simulations with
540 MODIS DOD in nine dusty regions. The seasonal cycle of gridded AERONET COD (as
541 an approximation to DOD; on a 0.5° by 0.5° grid) is also shown. Since the gridded COD
542 may have large uncertainties over regions with only a few stations, such as the Sahel,
543 Sahara, northern China, and South Africa, MODIS DOD is used as the main reference in
544 the comparison. Seasonal cycles are better captured by the $V_{\text{thresh12mn}}$ simulation in the
545 Sahel, the Sahara, and the Arabian Peninsula (Figs. 10a-c), although the spring and
546 summer peak in the Sahel is overestimated and winter minimum in the Sahara is
547 underestimated. The MAM peak of MODIS DOD in northern China is missed by both
548 $V_{\text{thresh12mn}}$ and $V_{\text{threshAnn}}$ simulations (Fig. 10d), while the JJA peak over India is
549 largely overestimated (Fig. 10e). Over the U.S. dusty region, the seasonal cycle in the



550 $V_{\text{thresh}12\text{mn}}$ simulation is slightly underestimated compared to MODIS DOD but
551 overestimated from May to August in the $V_{\text{thresh}Ann}$ simulation (Fig. 10f). DOD is
552 underestimated in South Africa in all three simulations (Fig. 10g). Over South America,
553 the peak from October to February is roughly captured by the $V_{\text{thresh}12\text{mn}}$ run but is
554 overestimated by the $V_{\text{thresh}Ann}$ run (Fig. 10h). The seasonal cycles of DOD in Australia
555 are very similar in all three simulations and largely resemble that in the MODIS, although
556 both the $V_{\text{thresh}12\text{mn}}$ and $V_{\text{thresh}Ann}$ simulations overestimate the DOD by about an order
557 of magnitude.

558 Figure 11 shows the seasonal cycle of COD from 12 AERONET SDA sites over
559 North Africa and nearby islands (see Figure S5 in the Supplement for site locations)
560 along with MODIS DOD and DOD simulated in three runs. The magnitude of
561 AERONET COD and MODIS DOD in these sites are very similar, despite missing values
562 at sites 1, 4, 5, 8, 11, and a smaller value at site 2 in MODIS. Over most of the sites, the
563 seasonal cycle is better captured in the $V_{\text{thresh}12\text{mn}}$ and $V_{\text{thresh}Ann}$ simulations than the
564 Control run, although the peak over Cairo_EMA_2 (site 12) is slightly underestimated,
565 which is consistent with the underestimation of annual mean DOD in the area (Fig. 6).

566 We also examined the seasonal cycle of PM₁₀ surface concentration at three
567 Sahelian INDAAF stations (see Figure S5 in the Supplement for site locations) from the
568 LISA project. Figures 12a-c show PM₁₀ surface dust concentration (here dust dominates
569 total PM₁₀ concentration) from the Control, $V_{\text{thresh}12\text{mn}}$, and $V_{\text{thresh}Ann}$ simulations
570 versus observed PM₁₀ concentration from three LISA sites. PM₁₀ concentrations in these
571 sites peak during boreal winter and spring and reach minima from July to September.
572 These seasonal variations are associated with the dry northerly Harmattan wind in boreal



573 winter that transports Saharan dust southward to the Guinean coast and the scavenging
574 effect of monsoonal rainfall in boreal summer that removes surface dust (Marticorena et
575 al., 2010). While the Control run does not capture the seasonal cycles in these sites, the
576 $V_{\text{thresh}12\text{mn}}$ run largely captures the spring peak and summer minimum, although the
577 magnitude is overestimated. In all three sites, the simulated concentration in the
578 $V_{\text{thresh}Ann}$ run is larger than that in the $V_{\text{thresh}12\text{mn}}$ run, especially in boreal fall to early
579 spring. Such an overestimation is probably due to the prescribed constant annual mean
580 $V_{\text{threshold}}$, which is lower than it would be during the less dusty season (i.e., boreal fall to
581 winter) and thus increases dust emission and surface concentration.

582 Figs. 12d-f show the seasonal cycle of DOD from three AERONET sites co-
583 located with LISA INDAAF stations and from three simulations. The $V_{\text{thresh}12\text{mn}}$ and
584 $V_{\text{thresh}Ann}$ simulations largely captured the seasonal cycle of DOD at these sites. The
585 overestimation of near surface PM_{10} dust concentration (Figs. 12a-c) and the generally
586 well-captured column integrated DOD (Figs. 12d-f) indicate that model likely
587 underestimates dust concentration in the atmospheric column above the surface, which
588 needs further investigation in future studies.

589

590 **3.2.4 A dust storm over U.S. northern Great Plains on October 18th, 2012**

591 Can the AM4.0/LM4.0 with prescribed $V_{\text{threshold}}$ better represent individual dust
592 events? Here we examine a major dust storm captured by MODIS Aqua true color-image
593 on Oct. 18th, 2012 (<https://earthobservatory.nasa.gov/images/79459/dust-storm-in-the-great-plains>)
594 over the U.S. northern Great Plains. There was a severe drought in 2012
595 with anomalously low precipitation centered over the central U.S. (e.g., Hoerling et al.,



596 2014). The dry conditions favored dust storm development when there were intensified
597 surface winds. However, this storm was not predicted by the forecast models, such as the
598 Goddard Earth Observing System version 5 (GEOS-5; Rienecker et al., 2008) and Navy
599 Aerosol Analysis Prediction System (NAAPS; Witek et al., 2007; Reid et al., 2009;
600 Westphal et al., 2009).

601 As shown in Figure 13, MODIS DOD also captures this event, with a peak value
602 above 0.5 over southwest Nebraska and northern Kansas on Oct. 18th, 2012. The
603 $V_{\text{thresh}12\text{mn}}$ run also largely captures this event (Fig. 13 bottom panel), although the
604 Control run totally misses it (not shown). In the model, the dust storm appears in South
605 Dakota and Nebraska on Oct. 17th, 2012, along with the anomalous southwesterly winds.
606 It reaches a maximum on Oct. 18th, in association with intensified anomalous
607 southwesterly winds at the surface and an anomalous low-pressure system at 850 hPa
608 (Figure S6 in the Supplement). Note that the modeled dust storm centers a bit
609 northeastward compared to the MODIS DOD pattern and it also has greater magnitude
610 and covers a larger area. On Oct. 19th, both the anomalous low-pressure system and
611 surface wind speeds weaken and the dust storm dissipates, with slightly elevated DOD
612 levels over a region extending over the lower Mississippi River basin and the Midwest.
613 This is somewhat consistent with MODIS records, which also shows slightly higher DOD
614 levels over Tennessee and northern Alabama on Oct. 19th, regardless of large area of
615 missing values.

616

617 **3.3 Frequency of DOD in the model versus that from MODIS**



618 Figure 14 shows the frequency of regional mean DOD during one dusty season
619 (MAM in the Northern Hemisphere and SON in the Southern Hemisphere) for nine
620 regions. Results from MODIS, the Control, and $V_{\text{thresh}}12\text{mn}$ runs are shown in black,
621 blue, and orange lines, respectively. In most dusty regions, such as the Sahara, Sahel,
622 Arabian Peninsula, India, and northern China, MODIS DOD frequency largely peaks
623 between 0.2 to 0.4, while DOD frequency peaks at a much lower level between 0.02 to
624 0.08 in less dusty regions, such as the U.S., South America, South Africa and Australia.
625 The DOD distribution in the Control run is biased low and peaks around 0.05 in those
626 dusty regions and between 0 and 0.01 in less dusty regions. The frequency is much better
627 captured in the $V_{\text{thresh}}12\text{mn}$ run over the Arabian Peninsula and the Sahel, slightly
628 improved but still biased low over the Sahara, northern China, India, and the U.S. The
629 modeled frequency in the $V_{\text{thresh}}12\text{mn}$ run is biased high in Australia (peaks outside the
630 maximum of x-axis, not shown) and shows little improvement over South Africa and
631 South America. The overall improvement of DOD frequency using the time-varying 2D
632 $V_{\text{threshold}}$ occurs mostly over major dusty regions, which is consistent with the
633 improvements in DOD climatology and seasonal cycle in the model simulations.

634

635 4. Discussion

636 A global distribution of the threshold of wind erosion is retrieved using high
637 resolution MODIS DOD and land surface constraints from relatively high-resolution
638 satellite products and reanalyses. While this climatological monthly $V_{\text{threshold}}$ provides
639 useful information about the spatial and temporal variations of wind erosion threshold,
640 there are some uncertainties associated with it. Here DOD frequency is derived using



641 MODIS and other satellite products, thus the uncertainties in the satellite products are
642 inherited in the derived DOD frequency distribution. Due to the cloud screening
643 processes of MODIS products, dust activities over cloud-covered regions may be
644 underestimated. Also, DOD frequency is derived based on daily observations over a 13-
645 year record, so that some variability of dust emission associated with alluvial sediments
646 deposited by seasonal flooding may be not captured. Diurnal variability of dust emission
647 and short-duration events such as haboobs are also not included. Since DOD is a column
648 integrated variable, it includes both local emitted and remotely transported dust. When
649 using DOD frequency distribution to approximate dust emission, it may overestimate dust
650 emission in regions where transported dust is dominated, e.g., over the southern Sahel,
651 and lead to an underestimation of $V_{threshold}$.

652 Previous study found that over regions such as North Africa, reanalysis products
653 may underestimate surface wind speed in spring and monsoon seasons but overestimate it
654 during dry nights (e.g., Largeron et al., 2015). This is largely because mechanisms such
655 as density current that can enhance surface wind speed are not parameterized in the
656 atmospheric models to produce the reanalysis products, while coarse spatial and temporal
657 sampling may also contribute to the underestimation of reanalysis wind speeds. These
658 limitations add uncertainties to the $V_{threshold}$ estimates derived here.

659 In addition, $V_{threshold}$ is derived by matching the frequency distribution of DOD at
660 certain levels (0.2 or 0.02) with the frequency distribution of daily maximum wind, and
661 these two values are derived empirically. The influences of soil properties such as soil
662 cohesion, particle size, and particle compositions on the threshold of wind erosion (e.g.,



663 Fécan et al., 1999; Alfaro and Gomes, 2001; Shao, 2001; Kok et al., 2014b) are not
664 explicitly examined here and will need further investigation.

665 The influences of $V_{threshold}$ on AM4.0/LM4.0 results are twofold. On the one hand,
666 it modifies the default constant threshold of wind erosion (V_i in Eq. 3) by allowing spatial
667 and temporal variations of wind erosion threshold over bare ground, i.e., within the
668 domain of default dust source function S (Figs. S7a-e in the Supplement). On the other
669 hand, it slightly extends the potential emission area to sparsely-vegetated regions as
670 outlined by $V_{threshold}$ (Figs. S7f-j in the Supplement). Which effect dominates? Taking the
671 $V_{thresh12mn}$ simulation as an example, Figure S8 shows the differences of dust emission
672 with the Control run. The increase of dust emission in the $V_{thresh12mn}$ simulation (also
673 summarized in Table S2 in the Supplement) is largely associated with the enhanced
674 emission over the bare ground (Figs. S8a-e in the Supplement), mainly over the regions
675 with reduced wind erosion threshold (Figs. S7a-e in the Supplement). The increased
676 emission over sparsely-vegetated area over regions such as the southern Sahel, India, and
677 Australia plays a minor role. This is consistent with Kim et al. (2013), who found global
678 dust emission in the Georgia Institute of Technology–Goddard Ozone Chemistry Aerosol
679 Radiation and Transport (GOCART) model is dominated by emission from bare ground.

680

681 **5. Conclusion**

682 While dust aerosols play important roles in the Earth's climate system, large
683 uncertainties exist in modeling its lifecycle (e.g., Huneeus et al., 2011; Pu and Ginoux,
684 2018b). Constant thresholds of wind erosion are widely used in climate models for
685 simplicity. Here, high-resolution MODIS Deep Blue dust optical depth (DOD) and



686 surface wind speeds from the NCEP1 reanalysis, along with other land surface factors
687 that affect wind erosion, such as soil moisture, vegetation cover, snow cover, soil
688 temperature, and soil depth, were used to develop a time-varying two-dimensional
689 climatological threshold of wind erosion, $V_{threshold}$, based on the seasonal variations of
690 DOD and surface wind distribution frequencies. $V_{threshold}$ is generally lower in dusty
691 seasons, i.e., MAM and JJA (SON and DJF) in the Northern (Southern) Hemisphere.
692 Globally, the lowest $V_{threshold}$ ($\sim 3\text{--}5\text{ m s}^{-1}$) is located over North Africa and the Arabian
693 Peninsula, with the highest values ($>10\text{ m s}^{-1}$) over northern Eurasia.

694 The climatological monthly $V_{threshold}$ was then incorporated into the GFDL
695 AM4.0/LM4.0 model to examine the potential benefits relative to the use of a constant
696 threshold. In comparison with the simulation using the default setting of a globally
697 constant threshold of wind erosion (6 m s^{-1}), the frequency distribution, magnitude, and
698 seasonal cycle of DOD are largely improved over Northern Hemisphere dusty regions,
699 such as North Africa and the Arabian Peninsula, and slightly improved over India, the
700 western to central U.S., and northern China. The magnitude and seasonal cycle of DOD
701 are also slightly improved in South America, although change little in South Africa. The
702 incorporation of $V_{threshold}$ leads to an overestimation of DOD in Australia, likely in
703 association with the absence of soil moisture constraints on dust emission in the model.

704 The overall underestimation of surface dust concentration under default model
705 setting is largely reduced when time-varying $V_{threshold}$ is incorporated, except over a
706 central Pacific island and a Icelandic island where the concentration is still
707 underestimated and over Australia and coastal China where dust concentration is
708 overestimated. The spatial pattern of surface fine dust concentration in the U.S. is also



709 better captured, with the maximum of annual mean largely located over the southwestern
710 U.S., although the magnitude is overestimated.

711 A constant annual mean $V_{threshold}$ is also tested in the model, and is found to
712 overestimate DOD over dusty seasons in the Arabian Peninsula, U.S., India, Australia,
713 and South America. Surface PM_{10} concentrations in the Sahel during boreal fall and
714 winter seasons are also largely overestimated with this setting. The results indicate the
715 importance of including the seasonal cycle of $V_{threshold}$ in the model. Using time-varying
716 $V_{threshold}$, the model was also able to capture a strong dust storm in the U.S. Great Plains
717 in October 2012, which created deadly accidents, while some dust forecasting models
718 failed to reproduce it.

719 Finally, this method to retrieve global threshold of wind erosion can be
720 conducted under different resolutions or surface wind reanalyses to match the resolution
721 of dust models and may help improve their simulations and forecasting of dust
722 distribution.

723

724

725

726

727

728

729

730

731



732 *Data availability.* Both the monthly and annual mean $V_{threshold}$ data at a 0.5° by 0.5°

733 resolution in NetCDF format is archived at: <https://www.gfdl.noaa.gov/pag->

734 [homepage/](#)

735

736 *Author contributions.* PG and BP conceived the study. PG processed the MODIS Deep

737 Blue aerosol data and guided model simulations. HG, SM, VN, ES, and MZ assisted with

738 model configurations, while CH, JK, BM, NO, CG, and JP provided guidance on data

739 usage and analysis. BP conducted model simulations, analyzed data and model results,

740 and wrote the paper with contributions from all other co-authors.

741

742 *Acknowledgements.*

743 This research is supported by NOAA and Princeton University's Cooperative

744 Institute for Climate Science and NASA under grant NNH14ZDA001N-ACMAP and

745 NNH16ZDA001N-MAP. The authors thank Drs. Veronica Chan and Hyeyum Shin for

746 their helpful comments on the early version of this paper and Dr. Sophie Vandebussche

747 for her valuable suggestions. We also thank the AERONET program for establishing and

748 maintaining the sunphotometer sites used in this study and the IMPROVE network for

749 the data. IMPROVE is a collaborative association of state, tribal, and federal agencies

750 and international partners. The US Environmental Protection Agency is the primary

751 funding source, with contracting and research support from the National Park Service.

752 The Air Quality Group at the University of California, Davis is the central analytical

753 laboratory, with ion analysis provided by Research Triangle Institute, and carbon analysis

754 provided by Desert Research Institute.



755 The AERONET aerosol optical depth data and SDA data are downloaded from

756 https://aeronet.gsfc.nasa.gov/new_web/download_all_v3_aod.html (last access: June

757 2018; Holben et al. 1998). IMPROVE fine dust data are downloaded from

758 <http://views.cira.colostate.edu/fed/DataWizard/> (last access: March 2017, Malm et al.,

759 1994; Hand et al., 2011).

760

761

762

763

764

765

766

767

768

769

770

771

772

773

774

775

776

777



- 778 Reference
779
780 Alfaro, S. C., and Gomes, L.: Modeling mineral aerosol production by wind erosion:
781 Emission intensities and aerosol size distributions in source areas, *J Geophys Res-*
782 *Atmos*, 106, 18075-18084, Doi 10.1029/2000jd900339, 2001.
- 783 Anderson, T. L., Wu, Y. H., Chu, D. A., Schmid, B., Redemann, J., and Dubovik, O.:
784 Testing the MODIS satellite retrieval of aerosol fine-mode fraction, *J Geophys*
785 *Res-Atmos*, 110, 10.1029/2005jd005978, 2005.
- 786 Andrews, E., Ogren, J. A., Kinne, S., and Samset, B.: Comparison of AOD, AOD and
787 column single scattering albedo from AERONET retrievals and in situ profiling
788 measurements, *Atmos Chem Phys*, 17, 6041-6072, 10.5194/acp-17-6041-2017,
789 2017.
- 790 Baddock, M. C., Ginoux, P., Bullard, J. E., and Gill, T. E.: Do MODIS-defined dust
791 sources have a geomorphological signature?, *Geophys Res Lett*, 43, 2606-2613,
792 10.1002/2015gl067327, 2016.
- 793 Bangert, M., Nenes, A., Vogel, B., Vogel, H., Barahona, D., Karydis, V. A., Kumar, P.,
794 Kottmeier, C., and Blahak, U.: Saharan dust event impacts on cloud formation
795 and radiation over Western Europe, *Atmos Chem Phys*, 12, 4045-4063,
796 10.5194/acp-12-4045-2012, 2012.
- 797 Barchyn, T. E., and Hugenholtz, C. H.: Comparison of four methods to calculate aeolian
798 sediment transport threshold from field data: Implications for transport prediction
799 and discussion of method evolution, *Geomorphology*, 129, 190-203,
800 10.1016/j.geomorph.2011.01.022, 2011.



- 801 Bentsen, M., Bethke, I., Debernard, J. B., Iversen, T., Kirkevåg, A., Seland, O., Drange,
802 H., Roelandt, C., Seierstad, I. A., Hoose, C., and Kristjansson, J. E.: The
803 Norwegian Earth System Model, NorESM1-M - Part 1: Description and basic
804 evaluation of the physical climate, *Geosci Model Dev*, 6, 687-720, 10.5194/gmd-
805 6-687-2013, 2013.
- 806 Bristow, C. S., Hudson-Edwards, K. A., and Chappell, A.: Fertilizing the Amazon and
807 equatorial Atlantic with West African dust, *Geophys Res Lett*, 37,
808 10.1029/2010gl043486, 2010.
- 809 Chomette, O., Legrand, M., and Marticorena, B.: Determination of the wind speed
810 threshold for the emission of desert dust using satellite remote sensing in the
811 thermal infrared, *J Geophys Res-Atmos*, 104, 31207-31215, Doi
812 10.1029/1999jd900756, 1999.
- 813 Collins, W. J., Bellouin, N., Doutriaux-Boucher, M., Gedney, N., Halloran, P., Hinton,
814 T., Hughes, J., Jones, C. D., Joshi, M., Liddicoat, S., Martin, G., O'Connor, F.,
815 Rae, J., Senior, C., Sitch, S., Totterdell, I., Wiltshire, A., and Woodward, S.:
816 Development and evaluation of an Earth-System model-HadGEM2, *Geosci
817 Model Dev*, 4, 1051-1075, 10.5194/gmd-4-1051-2011, 2011.
- 818 Cook, B. I., Miller, R. L., and Seager, R.: Dust and sea surface temperature forcing of the
819 1930s "Dust Bowl" drought, *Geophys Res Lett*, 35, 10.1029/2008gl033486, 2008.
- 820 Cook, B. I., Miller, R. L., and Seager, R.: Amplification of the North American "Dust
821 Bowl" drought through human-induced land degradation, *P Natl Acad Sci USA*,
822 106, 4997-5001, 10.1073/pnas.0810200106, 2009.



- 823 Cook, B. I., Seager, R., Miller, R. L., and Mason, J. A.: Intensification of North
824 American Megadroughts through Surface and Dust Aerosol Forcing, *J Climate*,
825 26, 4414-4430, 10.1175/Jcli-D-12-00022.1, 2013.
- 826 Cowie, S. M., Knippertz, P., and Marsham, J. H.: A climatology of dust emission events
827 from northern Africa using long-term surface observations, *Atmos Chem Phys*,
828 14, 8579-8597, 10.5194/acp-14-8579-2014, 2014.
- 829 Dee, D. P., Uppala, S. M., Simmons, A. J., Berrisford, P., Poli, P., Kobayashi, S., Andrae,
830 U., Balmaseda, M. A., Balsamo, G., Bauer, P., Bechtold, P., Beljaars, A. C. M.,
831 van de Berg, L., Bidlot, J., Bormann, N., Delsol, C., Dragani, R., Fuentes, M.,
832 Geer, A. J., Haimberger, L., Healy, S. B., Hersbach, H., Holm, E. V., Isaksen, L.,
833 Kallberg, P., Kohler, M., Matricardi, M., McNally, A. P., Monge-Sanz, B. M.,
834 Morcrette, J. J., Park, B. K., Peubey, C., de Rosnay, P., Tavolato, C., Thepaut, J.
835 N., and Vitart, F.: The ERA-Interim reanalysis: configuration and performance of
836 the data assimilation system, *Q J Roy Meteor Soc*, 137, 553-597, 10.1002/qj.828,
837 2011.
- 838 Donner, L. J., Wyman, B. L., Hemler, R. S., Horowitz, L. W., Ming, Y., Zhao, M., Golaz,
839 J. C., Ginoux, P., Lin, S. J., Schwarzkopf, M. D., Austin, J., Alaka, G., Cooke, W.
840 F., Delworth, T. L., Freidenreich, S. M., Gordon, C. T., Griffies, S. M., Held, I.
841 M., Hurlin, W. J., Klein, S. A., Knutson, T. R., Langenhorst, A. R., Lee, H. C.,
842 Lin, Y. L., Magi, B. I., Malyshev, S. L., Milly, P. C. D., Naik, V., Nath, M. J.,
843 Pincus, R., Ploshay, J. J., Ramaswamy, V., Seman, C. J., Shevliakova, E., Sirutis,
844 J. J., Stern, W. F., Stouffer, R. J., Wilson, R. J., Winton, M., Wittenberg, A. T.,
845 and Zeng, F. R.: The Dynamical Core, Physical Parameterizations, and Basic



- 846 Simulation Characteristics of the Atmospheric Component AM3 of the GFDL
847 Global Coupled Model CM3, *J Climate*, 24, 3484-3519, 10.1175/2011jcli3955.1,
848 2011.
- 849 Draxier, R. R., and Hess, G. D.: An overview of the HYSPLIT_4 modelling system for
850 trajectories, dispersion and deposition, *Aust Meteorol Mag*, 47, 295-308, 1998.
- 851 Draxler, R. R., Ginoux, P., and Stein, A. F.: An empirically derived emission algorithm
852 for wind-blown dust, *J Geophys Res-Atmos*, 115, 10.1029/2009jd013167, 2010.
- 853 Du, J., Jones, L. A., and Kimball, J. S.: Daily Global Land Parameters Derived from
854 AMSR-E and AMSR2, Version 2, <https://doi.org/10.5067/RF8WPYOPJKL2>,
855 2017a.
- 856 Du, J. Y., Kimball, J. S., Jones, L. A., Kim, Y., Glassy, J., and Watts, J. D.: A global
857 satellite environmental data record derived from AMSR-E and AMSR2
858 microwave Earth observations, *Earth Syst Sci Data*, 9, 791-808, 10.5194/essd-9-
859 791-2017, 2017b.
- 860 Dubovik, O., and King, M. D.: A flexible inversion algorithm for retrieval of aerosol
861 optical properties from Sun and sky radiance measurements, *J Geophys Res-*
862 *Atmos*, 105, 20673-20696, Doi 10.1029/2000jd900282, 2000.
- 863 Dumont, M., Brun, E., Picard, G., Michou, M., Libois, Q., Petit, J. R., Geyer, M., Morin,
864 S., and Josse, B.: Contribution of light-absorbing impurities in snow to
865 Greenland's darkening since 2009, *Nat Geosci*, 7, 509-512, 10.1038/Ngeo2180,
866 2014.
- 867 Dunion, J. P., and Velden, C. S.: The impact of the Saharan air layer on Atlantic tropical
868 cyclone activity, *B Am Meteorol Soc*, 85, 353-+, 10.1175/Bams-85-3-353, 2004.



- 869 Eck, T. F., Holben, B. N., Reid, J. S., Dubovik, O., Smirnov, A., O'Neill, N. T., Slutsker,
870 I., and Kinne, S.: Wavelength dependence of the optical depth of biomass
871 burning, urban, and desert dust aerosols, *J Geophys Res-Atmos*, 104, 31333-
872 31349, Doi 10.1029/1999jd900923, 1999.
- 873 Evan, A. T., Dunion, J., Foley, J. A., Heidinger, A. K., and Velden, C. S.: New evidence
874 for a relationship between Atlantic tropical cyclone activity and African dust
875 outbreaks, *Geophys Res Lett*, 33, 10.1029/2006gl026408, 2006.
- 876 Evans, S., Ginoux, P., Malyshev, S., and Shevliakova, E.: Climate-vegetation interaction
877 and amplification of Australian dust variability, *Geophys Res Lett*, 43, 11823-
878 11830, 10.1002/2016gl071016, 2016.
- 879 Fécan, F., Marticorena, B., and Bergametti, G.: Parametrization of the increase of the
880 aeolian erosion threshold wind friction velocity due to soil moisture for arid and
881 semi-arid areas, *Ann Geophys-Atm Hydr*, 17, 149-157, DOI
882 10.1007/s005850050744, 1999.
- 883 Fung, I. Y., Meyn, S. K., Tegen, I., Doney, S. C., John, J. G., and Bishop, J. K. B.: Iron
884 supply and demand in the upper ocean, *Global Biogeochem Cy*, 14, 281-295, Doi
885 10.1029/1999gb900059, 2000.
- 886 Gillette, D. A., Adams, J., Endo, A., Smith, D., and Kihl, R.: Threshold Velocities for
887 Input of Soil Particles into the Air by Desert Soils, *J Geophys Res-Oceans*, 85,
888 5621-5630, 10.1029/JC085iC10p05621, 1980.
- 889 Gillette, D. A., and Passi, R.: Modeling Dust Emission Caused by Wind Erosion, *J*
890 *Geophys Res-Atmos*, 93, 14233-14242, DOI 10.1029/JD093iD11p14233, 1988.



- 891 Ginoux, P., Chin, M., Tegen, I., Prospero, J. M., Holben, B., Dubovik, O., and Lin, S. J.:
892 Sources and distributions of dust aerosols simulated with the GOCART model, J
893 Geophys Res-Atmos, 106, 20255-20273, Doi 10.1029/2000jd000053, 2001.
- 894 Ginoux, P., Horowitz, L. W., Ramaswamy, V., Geogdzhayev, I. V., Holben, B. N.,
895 Stenchikov, G., and Tie, X.: Evaluation of aerosol distribution and optical depth
896 in the Geophysical Fluid Dynamics Laboratory coupled model CM2.1 for present
897 climate, J Geophys Res-Atmos, 111, 10.1029/2005jd006707, 2006.
- 898 Ginoux, P., Garbuzov, D., and Hsu, N. C.: Identification of anthropogenic and natural
899 dust sources using Moderate Resolution Imaging Spectroradiometer (MODIS)
900 Deep Blue level 2 data, J Geophys Res-Atmos, 115, 10.1029/2009jd012398,
901 2010.
- 902 Ginoux, P., Prospero, J. M., Gill, T. E., Hsu, N. C., and Zhao, M.: Global-Scale
903 Attribution of Anthropogenic and Natural Dust Sources and Their Emission Rates
904 Based on MODIS Deep Blue Aerosol Products, Rev Geophys, 50,
905 10.1029/2012rg000388, 2012.
- 906 Ginoux, P., and Deroubaix, A.: Space observations of dust in East Asia, Air pollution in
907 Eastern Asia: an integrated perspective, edited by: Bouarar, I., Wang, X., and
908 Brasseur, G. P., Springer, 2017.
- 909 Ginoux, P., Malyshev, S., Shevliakova, E., Chan, H. G., Guo, H., Milly, C., Naik, V.,
910 Pascale, S., Paulot, F., Pu, B., Zhao, M., and Kapnick, S.: Distribution of
911 absorbing aerosols in snow over high mountain ranges in GFDL AM4/LM4, in
912 preparation, 2019.



- 913 Hand, J. L., Copeland, S. A., Day, D. E., Dillner, A. M., Indresand, H., Malm, W. C.,
914 McDade, C. E., Moore, C. T., Pitchford, M. L., Schichtel, B. A., and Watson, J.
915 G.: IMPROVE (Interagency Monitoring of Protected Visual Environments):
916 Spatial and seasonal patterns and temporal variability of haze and its constituents
917 in the United States, 2011.
- 918 Hand, J. L., White, W. H., Gebhart, K. A., Hyslop, N. P., Gill, T. E., and Schichtel, B. A.:
919 Earlier onset of the spring fine dust season in the southwestern United States,
920 Geophys Res Lett, 43, 4001-4009, 10.1002/2016gl068519, 2016.
- 921 Hand, J. L., Gill, T. E., and Schichtel, B. A.: Spatial and seasonal variability in fine
922 mineral dust and coarse aerosol mass at remote sites across the United States, J
923 Geophys Res-Atmos, 122, 3080-3097, 10.1002/2016jd026290, 2017.
- 924 Helgren, D. M., and Prospero, J. M.: Wind Velocities Associated with Dust Deflation
925 Events in the Western Sahara, J Clim Appl Meteorol, 26, 1147-1151, Doi
926 10.1175/1520-0450(1987)026<1147:Wvawdd>2.0.Co;2, 1987.
- 927 Hoerling, M., Eischeid, J., Kumar, A., Leung, R., Mariotti, A., Mo, K., Schubert, S., and
928 Seager, R.: Causes and Predictability of the 2012 Great Plains Drought, B Am
929 Meteorol Soc, 95, 269-282, 10.1175/Bams-D-13-00055.1, 2014.
- 930 Holben, B. N., Eck, T. F., Slutsker, I., Tanre, D., Buis, J. P., Setzer, A., Vermote, E.,
931 Reagan, J. A., Kaufman, Y. J., Nakajima, T., Lavenu, F., Jankowiak, I., and
932 Smirnov, A.: AERONET - A federated instrument network and data archive for
933 aerosol characterization, Remote Sens Environ, 66, 1-16, Doi 10.1016/S0034-
934 4257(98)00031-5, 1998.



- 935 Holben, B. N., Eck, T. F., Slutsker, I., Smirnov, A., Sinyuk, A., Schafer, J., Giles, D., and
936 Dubovik, O.: AERONET's Version 2.0 quality assurance criteria, 2006.
- 937 Hsu, N. C., Tsay, S. C., King, M. D., and Herman, J. R.: Aerosol properties over bright-
938 reflecting source regions, *Ieee T Geosci Remote*, 42, 557-569,
939 10.1109/Tgrs.2004.824067, 2004.
- 940 Hsu, N. C., Jeong, M. J., Bettenhausen, C., Sayer, A. M., Hansell, R., Seftor, C. S.,
941 Huang, J., and Tsay, S. C.: Enhanced Deep Blue aerosol retrieval algorithm: The
942 second generation, *J Geophys Res-Atmos*, 118, 9296-9315, 10.1002/jgrd.50712,
943 2013.
- 944 Huneus, N., Schulz, M., Balkanski, Y., Griesfeller, J., Prospero, J., Kinne, S., Bauer, S.,
945 Boucher, O., Chin, M., Dentener, F., Diehl, T., Easter, R., Fillmore, D., Ghan, S.,
946 Ginoux, P., Grini, A., Horowitz, L., Koch, D., Krol, M. C., Landing, W., Liu, X.,
947 Mahowald, N., Miller, R., Morcrette, J. J., Myhre, G., Penner, J., Perlwitz, J.,
948 Stier, P., Takemura, T., and Zender, C. S.: Global dust model intercomparison in
949 AeroCom phase I, *Atmos Chem Phys*, 11, 7781-7816, 10.5194/acp-11-7781-
950 2011, 2011.
- 951 Jickells, T. D., An, Z. S., Andersen, K. K., Baker, A. R., Bergametti, G., Brooks, N., Cao,
952 J. J., Boyd, P. W., Duce, R. A., Hunter, K. A., Kawahata, H., Kubilay, N.,
953 laRoche, J., Liss, P. S., Mahowald, N., Prospero, J. M., Ridgwell, A. J., Tegen, I.,
954 and Torres, R.: Global iron connections between desert dust, ocean
955 biogeochemistry, and climate, *Science*, 308, 67-71, DOI
956 10.1126/science.1105959, 2005.



- 957 Jin, Q., Wei, J., Yang, Z. L., Pu, B., and Huang, J.: Consistent response of Indian summer
958 monsoon to Middle East dust in observations and simulations, *Atmos Chem Phys*,
959 15, 9897-9915, 10.5194/acp-15-9897-2015, 2015.
- 960 Jin, Q. J., Wei, J. F., and Yang, Z. L.: Positive response of Indian summer rainfall to
961 Middle East dust, *Geophys Res Lett*, 41, 4068-4074, 10.1002/2014gl059980,
962 2014.
- 963 Jin, Q. J., Yang, Z. L., and Wei, J. F.: Seasonal Responses of Indian Summer Monsoon to
964 Dust Aerosols in the Middle East, India, and China, *J Climate*, 29, 6329-6349,
965 10.1175/Jcli-D-15-0622.1, 2016.
- 966 Kalnay, E., Kanamitsu, M., Kistler, R., Collins, W., Deaven, D., Gandin, L., Iredell, M.,
967 Saha, S., White, G., Woollen, J., Zhu, Y., Chelliah, M., Ebisuzaki, W., Higgins,
968 W., Janowiak, J., Mo, K. C., Ropelewski, C., Wang, J., Leetmaa, A., Reynolds,
969 R., Jenne, R., and Joseph, D.: The NCEP/NCAR 40-year reanalysis project, *B Am*
970 *Meteorol Soc*, 77, 437-471, Doi 10.1175/1520-
971 0477(1996)077<0437:Tnyrp>2.0.Co;2, 1996.
- 972 Kim, D., Chin, M. A., Bian, H. S., Tan, Q., Brown, M. E., Zheng, T., You, R. J., Diehl,
973 T., Ginoux, P., and Kucsera, T.: The effect of the dynamic surface bareness on
974 dust source function, emission, and distribution, *J Geophys Res-Atmos*, 118, 871-
975 886, 10.1029/2012jd017907, 2013.
- 976 Kim, M. K., Lau, W. K. M., Kim, K. M., Sang, J., Kim, Y. H., and Lee, W. S.:
977 Amplification of ENSO effects on Indian summer monsoon by absorbing
978 aerosols, *Clim Dynam*, 46, 2657-2671, 10.1007/s00382-015-2722-y, 2016.



- 979 Kok, J. F., Albani, S., Mahowald, N. M., and Ward, D. S.: An improved dust emission
980 model - Part 2: Evaluation in the Community Earth System Model, with
981 implications for the use of dust source functions, Atmos Chem Phys, 14, 13043-
982 13061, 10.5194/acp-14-13043-2014, 2014a.
- 983 Kok, J. F., Mahowald, N. M., Fratini, G., Gillies, J. A., Ishizuka, M., Leys, J. F., Mikami,
984 M., Park, M. S., Park, S. U., Van Pelt, R. S., and Zobeck, T. M.: An improved
985 dust emission model - Part 1: Model description and comparison against
986 measurements, Atmos Chem Phys, 14, 13023-13041, 10.5194/acp-14-13023-
987 2014, 2014b.
- 988 Kurosaki, Y., and Mikami, M.: Effect of snow cover on threshold wind velocity of dust
989 outbreak, Geophys Res Lett, 31, 10.1029/2003gl018632, 2004.
- 990 Kurosaki, Y., and Mikami, M.: Threshold wind speed for dust emission in east Asia and
991 its seasonal variations, J Geophys Res-Atmos, 112, 10.1029/2006jd007988, 2007.
- 992 Llargeron, Y., Guichard, F., Bouniol, D., Couvreur, F., Kergoat, L., and Marticorena, B.:
993 Can we use surface wind fields from meteorological reanalyses for Sahelian dust
994 emission simulations?, Geophys Res Lett, 42, 2490-2499, 10.1002/2014gl062938,
995 2015.
- 996 Levin, Z., Ganor, E., and Gladstein, V.: The effects of desert particles coated with sulfate
997 on rain formation in the eastern Mediterranean, J Appl Meteorol, 35, 1511-1523,
998 Doi 10.1175/1520-0450(1996)035<1511:Teodpc>2.0.Co;2, 1996.
- 999 Lin, C. Y., Zhao, C., Liu, X. H., Lin, N. H., and Chen, W. N.: Modelling of long-range
1000 transport of Southeast Asia biomass-burning aerosols to Taiwan and their
1001 radiative forcings over East Asia, Tellus B, 66, 10.3402/tellusb.v66.23733, 2014.



- 1002 Mahowald, N. M., Baker, A. R., Bergametti, G., Brooks, N., Duce, R. A., Jickells, T. D.,
1003 Kubilay, N., Prospero, J. M., and Tegen, I.: Atmospheric global dust cycle and
1004 iron inputs to the ocean, *Global Biogeochem Cy*, 19, 10.1029/2004gb002402,
1005 2005.
- 1006 Mahowald, N. M., Kloster, S., Engelstaedter, S., Moore, J. K., Mukhopadhyay, S.,
1007 McConnell, J. R., Albani, S., Doney, S. C., Bhattacharya, A., Curran, M. A. J.,
1008 Flanner, M. G., Hoffman, F. M., Lawrence, D. M., Lindsay, K., Mayewski, P. A.,
1009 Neff, J., Rothenberg, D., Thomas, E., Thornton, P. E., and Zender, C. S.:
1010 Observed 20th century desert dust variability: impact on climate and
1011 biogeochemistry, *Atmos Chem Phys*, 10, 10875-10893, 10.5194/acp-10-10875-
1012 2010, 2010.
- 1013 Malm, W. C., Sisler, J. F., Huffman, D., Eldred, R. A., and Cahill, T. A.: Spatial and
1014 Seasonal Trends in Particle Concentration and Optical Extinction in the United-
1015 States, *J Geophys Res-Atmos*, 99, 1347-1370, Doi 10.1029/93jd02916, 1994.
- 1016 Marsham, J. H., Hobby, M., Allen, C. J. T., Banks, J. R., Bart, M., Brooks, B. J.,
1017 Cavazos-Guerra, C., Engelstaedter, S., Gascoyne, M., Lima, A. R., Martins, J. V.,
1018 McQuaid, J. B., O'Leary, A., Ouchene, B., Ouladichir, A., Parker, D. J., Saci, A.,
1019 Salah-Ferroudj, M., Todd, M. C., and Washington, R.: Meteorology and dust in
1020 the central Sahara: Observations from Fennec supersite-1 during the June 2011
1021 Intensive Observation Period, *J Geophys Res-Atmos*, 118, 4069-4089,
1022 10.1002/jgrd.50211, 2013.



- 1023 Marticorena, B., and Bergametti, G.: Modeling the Atmospheric Dust Cycle .1. Design of
1024 a Soil-Derived Dust Emission Scheme, *J Geophys Res-Atmos*, 100, 16415-16430,
1025 Doi 10.1029/95jd00690, 1995.
- 1026 Marticorena, B., Bergametti, G., Aumont, B., Callot, Y., NDoume, C., and Legrand, M.:
1027 Modeling the atmospheric dust cycle .2. Simulation of Saharan dust sources, *J*
1028 *Geophys Res-Atmos*, 102, 4387-4404, Doi 10.1029/96jd02964, 1997.
- 1029 Marticorena, B., Chatenet, B., Rajot, J. L., Traore, S., Coulibaly, M., Diallo, A., Kone, I.,
1030 Maman, A., Diaye, T. N., and Zakou, A.: Temporal variability of mineral dust
1031 concentrations over West Africa: analyses of a pluriannual monitoring from the
1032 AMMA Sahelian Dust Transect, *Atmos Chem Phys*, 10, 8899-8915, 10.5194/acp-
1033 10-8899-2010, 2010.
- 1034 Miller, R. L., and Tegen, I.: Climate response to soil dust aerosols, *J Climate*, 11, 3247-
1035 3267, Doi 10.1175/1520-0442(1998)011<3247:Crtsda>2.0.Co;2, 1998.
- 1036 Miller, R. L., Tegen, I., and Perlwitz, J.: Surface radiative forcing by soil dust aerosols
1037 and the hydrologic cycle, *J Geophys Res-Atmos*, 109, 10.1029/2003jd004085,
1038 2004.
- 1039 Moorthi, S., and Suarez, M. J.: Relaxed Arakawa-Schubert - a Parameterization of Moist
1040 Convection for General-Circulation Models, *Mon Weather Rev*, 120, 978-1002,
1041 Doi 10.1175/1520-0493(1992)120<0978:Rasapo>2.0.Co;2, 1992.
- 1042 Naik, V., Horowitz, L. W., Fiore, A. M., Ginoux, P., Mao, J. Q., Aghedo, A. M., and
1043 Levy, H.: Impact of preindustrial to present-day changes in short-lived pollutant
1044 emissions on atmospheric composition and climate forcing, *J Geophys Res-*
1045 *Atmos*, 118, 8086-8110, 10.1002/jgrd.50608, 2013.



- 1046 Nakajima, T., Higurashi, A., Kawamoto, K., and Penner, J. E.: A possible correlation
1047 between satellite-derived cloud and aerosol microphysical parameters, *Geophys*
1048 *Res Lett*, 28, 1171-1174, Doi 10.1029/2000gl012186, 2001.
- 1049 O'Neill, N. T., Eck, T. F., Smirnov, A., Holben, B. N., and Thulasiraman, S.: Spectral
1050 discrimination of coarse and fine mode optical depth, *J Geophys Res-Atmos*, 108,
1051 10.1029/2002jd002975, 2003.
- 1052 Painter, T. H., Deems, J. S., Belnap, J., Hamlet, A. F., Landry, C. C., and Udall, B.:
1053 Response of Colorado River runoff to dust radiative forcing in snow, *P Natl Acad*
1054 *Sci USA*, 107, 17125-17130, 10.1073/pnas.0913139107, 2010.
- 1055 Painter, T. H., Skiles, S. M., Deems, J. S., Brandt, W. T., and Dozier, J.: Variation in
1056 Rising Limb of Colorado River Snowmelt Runoff Hydrograph Controlled by Dust
1057 Radiative Forcing in Snow, *Geophys Res Lett*, 45, 797-808,
1058 10.1002/2017gl075826, 2018.
- 1059 Pu, B., and Ginoux, P.: The impact of the Pacific Decadal Oscillation on springtime dust
1060 activity in Syria, *Atmos Chem Phys*, 16, 13431-13448, 10.5194/acp-16-13431-
1061 2016, 2016.
- 1062 Pu, B., and Ginoux, P.: Projection of American dustiness in the late 21st century due to
1063 climate change, *Scientific reports*, 7, 10.1038/s41598-017-05431-9, 2017.
- 1064 Pu, B., and Ginoux, P.: Climatic factors contributing to long-term variations in surface
1065 fine dust concentration in the United States, *Atmos Chem Phys*, 18, 4201-4215,
1066 10.5194/acp-18-4201-2018, 2018a.



- 1067 Pu, B., and Ginoux, P.: How reliable are CMIP5 models in simulating dust optical
1068 depth?, Atmos Chem Phys, 18, 12491-12510, 10.5194/acp-18-12491-2018,
1069 2018b.
- 1070 Putman, W. M., and Lin, S. H.: Finite-volume transport on various cubed-sphere grids, J
1071 Comput Phys, 227, 55-78, 10.1016/j.jcp.2007.07.022, 2007.
- 1072 Raupach, M. R., Gillette, D. A., and Leys, J. F.: The Effect of Roughness Elements on
1073 Wind Erosion Threshold, J Geophys Res-Atmos, 98, 3023-3029, Doi
1074 10.1029/92jd01922, 1993.
- 1075 Rayner, N. A., Parker, D. E., Horton, E. B., Folland, C. K., Alexander, L. V., Rowell, D.
1076 P., Kent, E. C., and Kaplan, A.: Global analyses of sea surface temperature, sea
1077 ice, and night marine air temperature since the late nineteenth century, J Geophys
1078 Res-Atmos, 108, 10.1029/2002jd002670, 2003.
- 1079 Reid, J. S., Hyer, E. J., Prins, E. M., Westphal, D. L., Zhang, J. L., Wang, J., Christopher,
1080 S. A., Curtis, C. A., Schmidt, C. C., Eleuterio, D. P., Richardson, K. A., and
1081 Hoffman, J. P.: Global Monitoring and Forecasting of Biomass-Burning Smoke:
1082 Description of and Lessons From the Fire Locating and Modeling of Burning
1083 Emissions (FLAMBE) Program, Ieee J-Stars, 2, 144-162,
1084 10.1109/Jstars.2009.2027443, 2009.
- 1085 Reynolds, R. W., Rayner, N. A., Smith, T. M., Stokes, D. C., and Wang, W. Q.: An
1086 improved in situ and satellite SST analysis for climate, J Climate, 15, 1609-1625,
1087 Doi 10.1175/1520-0442(2002)015<1609:Aiisas>2.0.Co;2, 2002.
- 1088 Rienecker, M. M., Suarez, M. J., Todling, R., Bacmeister, J., Takacs, L., Liu, H.-C., Gu,
1089 W., Sienkiewicz, M., Koster, R. D., Gelaro, R., Stajner, I., and Nielsen, J. E.: The



- 1090 GEOS - 5 Data Assimilation System—Documentation of versions 5.0.1, 5.1.0, and
1091 5.2.0, Technical Report Series on Global Modeling and Data Assimilation, 27
1092 (available at <http://gmao.gsfc.nasa.gov/pubs/docs/Rienecker369.pdf>), 2008.
- 1093 Rosenfield, J. E., Considine, D. B., Meade, P. E., Bacmeister, J. T., Jackman, C. H., and
1094 Schoeberl, M. R.: Stratospheric effects of Mount Pinatubo aerosol studied with a
1095 coupled two-dimensional model, *J Geophys Res-Atmos*, 102, 3649-3670, Doi
1096 10.1029/96jd03820, 1997.
- 1097 Savoie, D. L., and Prospero, J. M.: Comparison of Oceanic and Continental Sources of
1098 Non-Sea-Salt Sulfate over the Pacific-Ocean, *Nature*, 339, 685-687, DOI
1099 10.1038/339685a0, 1989.
- 1100 Sayer, A. M., Hsu, N. C., Bettenhausen, C., and Jeong, M. J.: Validation and uncertainty
1101 estimates for MODIS Collection 6 "Deep Blue" aerosol data, *J Geophys Res-*
1102 *Atmos*, 118, 7864-7872, 10.1002/jgrd.50600, 2013.
- 1103 Shao, Y.: A model for mineral dust emission, *J Geophys Res-Atmos*, 106, 20239-20254,
1104 Doi 10.1029/2001jd900171, 2001.
- 1105 Shao, Y. P., Wyrwoll, K. H., Chappell, A., Huang, J. P., Lin, Z. H., McTainsh, G. H.,
1106 Mikami, M., Tanaka, T. Y., Wang, X. L., and Yoon, S.: Dust cycle: An emerging
1107 core theme in Earth system science, *Aeolian Res*, 2, 181-204,
1108 10.1016/j.aeolia.2011.02.001, 2011.
- 1109 Sharma, D., and Miller, R. L.: Revisiting the observed correlation between weekly
1110 averaged Indian monsoon precipitation and Arabian Sea aerosol optical depth,
1111 *Geophys Res Lett*, 44, 10006-10016, 10.1002/2017gl074373, 2017.



- 1112 Solmon, F., Nair, V. S., and Mallet, M.: Increasing Arabian dust activity and the Indian
1113 summer monsoon, *Atmos Chem Phys*, 15, 8051-8064, 10.5194/acp-15-8051-
1114 2015, 2015.
- 1115 Strong, J. D., Vecchi, G. A., and Ginoux, P.: The Climatological Effect of Saharan Dust
1116 on Global Tropical Cyclones in a Fully Coupled GCM, *Journal of Geophysical
1117 Research - Atmospheres*, 123, <https://doi.org/10.1029/2017JD027808>, 2018.
- 1118 Strong, J. D. O., Vecchi, G. A., and Ginoux, P.: The Response of the Tropical Atlantic
1119 and West African Climate to Saharan Dust in a Fully Coupled GCM, *J Climate*,
1120 28, 7071-7092, 10.1175/Jcli-D-14-00797.1, 2015.
- 1121 Takemura, T., Okamoto, H., Maruyama, Y., Numaguti, A., Higurashi, A., and Nakajima,
1122 T.: Global three-dimensional simulation of aerosol optical thickness distribution
1123 of various origins, *J Geophys Res-Atmos*, 105, 17853-17873, Doi
1124 10.1029/2000jd900265, 2000.
- 1125 Taylor, K., Williamson, D., and Zwiers, F.: The sea surface temperature and sea ice
1126 concentration boundary conditions for AMIP II simulations (PCMDI Rep. 60, pp.
1127 1–25), Livermore, CA:Program for Climate Model Diagnosis and
1128 Intercomparison, Lawrence Livermore National Laboratory, 2000.
- 1129 Tegen, I., and Fung, I.: Modeling of Mineral Dust in the Atmosphere - Sources,
1130 Transport, and Optical-Thickness, *J Geophys Res-Atmos*, 99, 22897-22914, Doi
1131 10.1029/94jd01928, 1994.
- 1132 Tong, D. Q., Wang, J. X. L., Gill, T. E., Lei, H., and Wang, B. Y.: Intensified dust storm
1133 activity and Valley fever infection in the southwestern United States, *Geophys
1134 Res Lett*, 44, 4304-4312, 10.1002/2017gl073524, 2017.



- 1135 Uno, I., Amano, H., Emori, S., Kinoshita, K., Matsui, I., and Sugimoto, N.: Trans-Pacific
1136 yellow sand transport observed in April 1998: A numerical simulation, *J Geophys*
1137 *Res-Atmos*, 106, 18331-18344, Doi 10.1029/2000jd900748, 2001.
- 1138 Vinoj, V., Rasch, P. J., Wang, H. L., Yoon, J. H., Ma, P. L., Landu, K., and Singh, B.:
1139 Short-term modulation of Indian summer monsoon rainfall by West Asian dust,
1140 *Nat Geosci*, 7, 308-313, 10.1038/ngeo2107, 2014.
- 1141 Watanabe, S., Hajima, T., Sudo, K., Nagashima, T., Takemura, T., Okajima, H., Nozawa,
1142 T., Kawase, H., Abe, M., Yokohata, T., Ise, T., Sato, H., Kato, E., Takata, K.,
1143 Emori, S., and Kawamiya, M.: MIROC-ESM 2010: model description and basic
1144 results of CMIP5-20c3m experiments, *Geosci Model Dev*, 4, 845-872,
1145 10.5194/gmd-4-845-2011, 2011.
- 1146 Westphal, D. L., Curtis, C. A., Liu, M., and Walker, A. L.: Operational aerosol and dust
1147 storm forecasting, in *WMO/GEO Expert Meeting on an International Sand and*
1148 *Dust Storm Warning System*, IOP Conference Series Earth and Environmental
1149 Science, 2009.
- 1150 Witek, M. L., Flatau, P. J., Quinn, P. K., and Westphal, D. L.: Global sea-salt modeling:
1151 Results and validation against multicampaign shipboard measurements, *J*
1152 *Geophys Res-Atmos*, 112, Artn D08215
1153 10.1029/2006jd007779, 2007.
- 1154 Wong, S., and Dessler, A. E.: Suppression of deep convection over the tropical North
1155 Atlantic by the Saharan Air Layer, *Geophys Res Lett*, 32, 10.1029/2004gl022295,
1156 2005.



- 1157 Wurzler, S., Reisin, T. G., and Levin, Z.: Modification of mineral dust particles by cloud
1158 processing and subsequent effects on drop size distributions, *J Geophys Res-*
1159 *Atmos*, 105, 4501-4512, Doi 10.1029/1999jd900980, 2000.
- 1160 Yu, H. B., Chin, M., Yuan, T. L., Bian, H. S., Remer, L. A., Prospero, J. M., Omar, A.,
1161 Winker, D., Yang, Y. K., Zhang, Y., Zhang, Z. B., and Zhao, C.: The fertilizing
1162 role of African dust in the Amazon rainforest: A first multiyear assessment based
1163 on data from Cloud-Aerosol Lidar and Infrared Pathfinder Satellite Observations,
1164 *Geophys Res Lett*, 42, 1984-1991, 10.1002/2015gl063040, 2015.
- 1165 Zender, C. S., Bian, H. S., and Newman, D.: Mineral Dust Entrainment and Deposition
1166 (DEAD) model: Description and 1990s dust climatology, *J Geophys Res-Atmos*,
1167 108, 10.1029/2002jd002775, 2003.
- 1168 Zhao, M., Golaz, J. C., Held, I. M., Guo, H., Balaji, V., Benson, R., Chen, J. H., Chen,
1169 X., Donner, L. J., Dunne, J. P., Dunne, K., Durachta, J., Fan, S. M., Freidenreich,
1170 S. M., Garner, S. T., Ginoux, P., Harris, L. M., Horowitz, L. W., Krasting, J. P.,
1171 Langenhorst, A. R., Liang, Z., Lin, P., Lin, S. J., Malyshev, S. L., Mason, E.,
1172 Milly, P. C. D., Ming, Y., Naik, V., Paulot, F., Paynter, D., Phillipps, P.,
1173 Radhakrishnan, A., Ramaswamy, V., Robinson, T., Schwarzkopf, D., Seman, C.
1174 J., Shevliakova, E., Shen, Z., Shin, H., Silvers, L. G., Wilson, J. R., Winton, M.,
1175 Wittenberg, A. T., Wyman, B., and Xiang, B.: The GFDL Global Atmosphere and
1176 Land Model AM4.0/LM4.0:1. Simulation Characteristics With Prescribed SSTs, *J*
1177 *Adv Model Earth Sy*, 10, 691-734, 10.1002/2017ms001208, 2018a.
- 1178 Zhao, M., Golaz, J. C., Held, I. M., Guo, H., Balaji, V., Benson, R., Chen, J. H., Chen,
1179 X., Donner, L. J., Dunne, J. P., Dunne, K., Durachta, J., Fan, S. M., Freidenreich,



1180 S. M., Garner, S. T., Ginoux, P., Harris, L. M., Horowitz, L. W., Krasting, J. P.,
1181 Langenhorst, A. R., Liang, Z., Lin, P., Lin, S. J., Malyshev, S. L., Mason, E.,
1182 Milly, P. C. D., Ming, Y., Naik, V., Paulot, F., Paynter, D., Phillipps, P.,
1183 Radhakrishnan, A., Ramaswamy, V., Robinson, T., Schwarzkopf, D., Seman, C.
1184 J., Shevliakova, E., Shen, Z., Shin, H., Silvers, L. G., Wilson, J. R., Winton, M.,
1185 Wittenberg, A. T., Wyman, B., and Xiang, B.: The GFDL Global Atmosphere and
1186 Land Model AM4.0/LM4.0.2. Model Description, Sensitivity Studies, and Tuning
1187 Strategies, *J Adv Model Earth Sy*, 10, 735-769, 10.1002/2017ms001209, 2018b.
1188



1189 Table 1 Major dusty regions shown in Figure 1. Note that region names such as India and
1190 northern China are not exactly the same as their geographical definitions but also cover
1191 some areas from nearby countries.

1192

1193 Table 2 Simulation design

1194

1195

1196

1197

1198

1199

1200

1201

1202

1203

1204

1205

1206

1207

1208

1209

1210

1211



1212 Figure 1. (a)-(e) Frequencies of occurrence (FoO; unit: days per season)
1213 and annual mean. (f)-(j) Threshold of wind erosion ($V_{threshold}$; unit: m s^{-1}) derived from
1214 satellite products and reanalyses for each season and annual mean. Black boxes in (f)
1215 denote nine dusty regions as listed in Table 1.

1216

1217 Figure 2. (a) Cumulative frequency of $V_{threshold}$ over global land for each season (black,
1218 orange, blue, green, and grey lines denote annual, SON, JJA, MAM, and DJF averages,
1219 respectively). Color dashed lines correspond to the percentages of $V_{threshold} = 6 \text{ m s}^{-1}$ for
1220 each season and annual mean. Color arrows point to the value of $V_{threshold}$ at the 50% level
1221 in each season and annual mean. (b)-(i) distribution of annual mean $V_{threshold}$ (black bars)
1222 in each region (black boxes in Fig. 1) and for dusty seasons, i.e., MAM (green) and JJA
1223 (blue) for regions in the Northern Hemisphere and SON (orange) and DJF (grey) for
1224 regions in the Southern Hemisphere. The mean and \pm one standard deviations of $V_{threshold}$
1225 in each region are shown on the top right of each plot.

1226

1227 Figure 3. Climatology of annual mean AERONET (a) AOD (550 nm) and (b) SDA COD
1228 (500 nm) averaged over 2003-2015.

1229

1230 Figure 4. Scatter plot of simulated annual mean (a) AOD and (b) COD in the Control run
1231 versus AERONET AOD and COD (left), and the relative difference (in percentage) (c)
1232 between modeled AOD and AERONET AOD and (d) between modeled COD and
1233 AERONET COD (right). (e) The relative contribution of DOD to COD in the model.

1234



1235 Figure 5. Same as Fig. 4 but for the $V_{\text{thresh}}12\text{mn}$ simulation.

1236

1237 Figure 6. (a) Climatology (2003-2015) of AERONET DOD (550 nm) over major dusty
1238 regions and (b) scatter plot of modeled DOD in the $V_{\text{thresh}}12\text{mn}$ simulation versus
1239 AERONET DOD, and (c) the relative difference (in percentage) between modeled DOD
1240 and AERONET DOD in the $V_{\text{thresh}}12\text{mn}$ simulation.

1241

1242 Figure 7. Regional averaged annual mean DOD (2003-2015) over nine regions from the
1243 Control (grey), $V_{\text{thresh}}12\text{mn}$ (orange), and $V_{\text{thresh}}\text{Ann}$ (yellow) simulations and MODIS
1244 (black).

1245

1246 Figure 8. Scatter plots (left column) of model simulated (from top to bottom are the
1247 Control, $V_{\text{thresh}}\text{Ann}$, and $V_{\text{thresh}}12\text{mn}$ simulations) surface dust concentration versus the
1248 climatology of observed surface dust concentration from RSMAS stations (Savoie and
1249 Prospero 1989), and spatial pattern of surface dust concentration from model output
1250 (shading; right column) and the ratio between modeled and RSMAS station observed
1251 surface dust concentration (color triangles, with upward triangles indicating
1252 overestimation and downward triangles indicating underestimation). 16 stations were
1253 used, and numbers in each triangle (right) and grey dots (left) indicate the stations. The
1254 one-one, one-two and one-five lines are plotted in solid, dashed and dash-dotted lines in
1255 the scatter plots.

1256



1257 Figure 9. Annual mean surface fine dust concentration ($\mu\text{g m}^{-3}$) from IMPROVE stations
1258 (left column) and three simulations (middle column) and the differences between model
1259 and observation (right column) for 2002-2015.

1260

1261 Figure 10. Seasonal cycle of DOD from MODIS (black), the Control (grey), $V_{\text{thresh}12\text{mn}}$
1262 (orange), and $V_{\text{thresh}Ann}$ (yellow) runs, and gridded AERONET SDA COD (blue)
1263 averaged over nine regions. The annual mean of each dataset in each region is listed on
1264 the top of the plot.

1265

1266 Figure 11. Seasonal cycle of DOD over 12 AERONET SDA sites (see Fig. S5 in the
1267 Supplement for locations) from the Control (grey), $V_{\text{thresh}12\text{mn}}$ (orange), and $V_{\text{thresh}Ann}$
1268 (yellow) simulations, along with DOD from MODIS (blue), and COD from AERONET
1269 (black dotted line). All values are averaged over 2003-2015. The location (lat/long) and
1270 the name (due to space, only first seven characters are shown) of the sites are listed at the
1271 top of each plot.

1272

1273 Figure 12. (a)-(c) Seasonal cycle of PM_{10} surface concentration (black) over three sites
1274 from the LISA project, along with PM_{10} surface dust concentration from the Control
1275 (grey), $V_{\text{thresh}12\text{mn}}$ (orange), and $V_{\text{thresh}Ann}$ (yellow) simulations. Error bars are \pm one
1276 standard deviations of daily mean in each month averaged over 2006-2014. Unites: $\mu\text{g m}^{-3}$.
1277 ³. (d)-(f) seasonal cycle of DOD (550 nm) from three AERONET sites co-located with
1278 LISA sites (blue) versus that modeled by the Control (grey), $V_{\text{thresh}12\text{mn}}$ (orange), and
1279 $V_{\text{thresh}Ann}$ (yellow) simulations.



1280 Figure 13. Daily DOD from MODIS (top panel), daily DOD simulated by the $V_{\text{thresh}12\text{mn}}$
1281 run along with anomalies (with reference to the 2000-2015 mean) of surface wind vectors
1282 (m s^{-1} ; bottom panel) from Oct. 17th to Oct. 19th, 2012. Only DOD over land is shown.
1283 Missing values in MODIS DOD (top panel) are plotted in grey shading.

1284

1285 Figure 14. Frequency (%) distribution of regional averaged daily DOD from MODIS
1286 (black) versus that from the Control (light blue) and $V_{\text{thresh}12\text{mn}}$ (orange) simulations for
1287 the Sahara, the Sahel, the Arabian Peninsula, northern China, India, western to central
1288 U.S., South America, South Africa, and Australia from 2003 to 2015. X-axis denotes the
1289 ranges of DOD, and y-axis is percentage of occurrence. The light green boxes denote the
1290 averaging areas. For regions in the Northern Hemisphere frequency in MAM is shown,
1291 while for regions in the Southern Hemisphere frequency in SON is shown.

1292

1293

1294

1295

1296

1297

1298

1299

1300

1301

1302



1303 Table 1 Major dusty regions shown in Figure 1. Note that region names such as India and
 1304 northern China are not exactly the same as their geographical definitions but also cover
 1305 some areas from nearby countries.
 1306

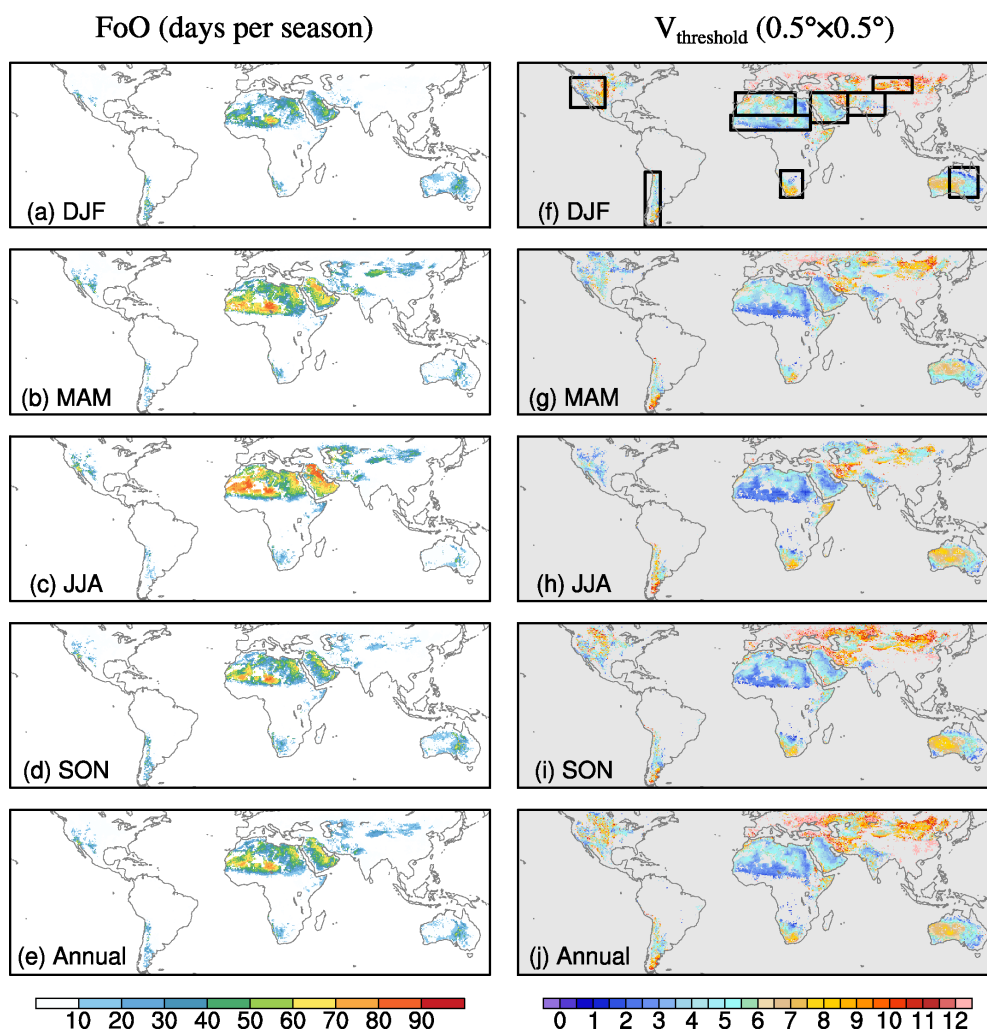
No.	Regions	Lat/long
1	Sahel	10°-20°N, 18°W-35°E
2	Sahara	20°-35°N, 15°W-25°E
3	Arabian Peninsula	15°-35°N, 35°-60°E
4	Northern China (N. China)	35°-45°N, 77°-103°E
5	India	20°-35°N, 60°-85°E
6	U.S.	25°-45°N, 102°-125°W
7	South Africa (S. Africa)	17°-35°S, 15°-30°E
8	South America (S. America)	18°-55°S, 65°-75°W
9	Australia	15°-35°S, 128-147°E

1307
 1308
 1309
 1310
 1311
 1312

Table 2 Simulation design

Simulations	Wind erosion threshold	Source function
Control	6 m s ⁻¹	<i>S</i>
V _{thresh} 12mn	12-month <i>V_{threshold}</i>	<i>S'</i>
V _{thresh} Ann	Annual mean <i>V_{threshold}</i>	<i>S'</i>

1313
 1314
 1315
 1316



1317

1318

1319 Figure 1. (a)-(e) Frequencies of occurrence (FoO; unit: days per season) in each season

1320 and annual mean. (f)-(j) Threshold of wind erosion ($V_{threshold}$; unit: m s^{-1}) derived from

1321 satellite products and reanalyses for each season and annual mean. Black boxes in (f)

1322

1323

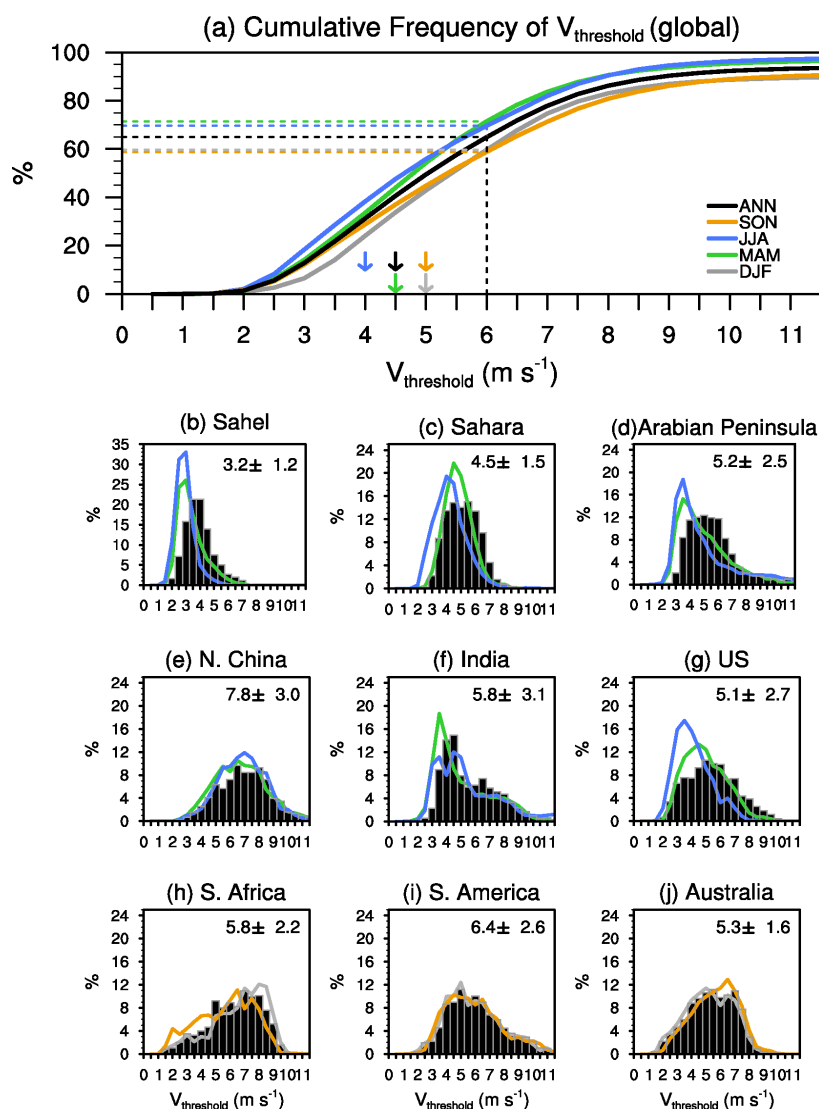
1324

1325

1326

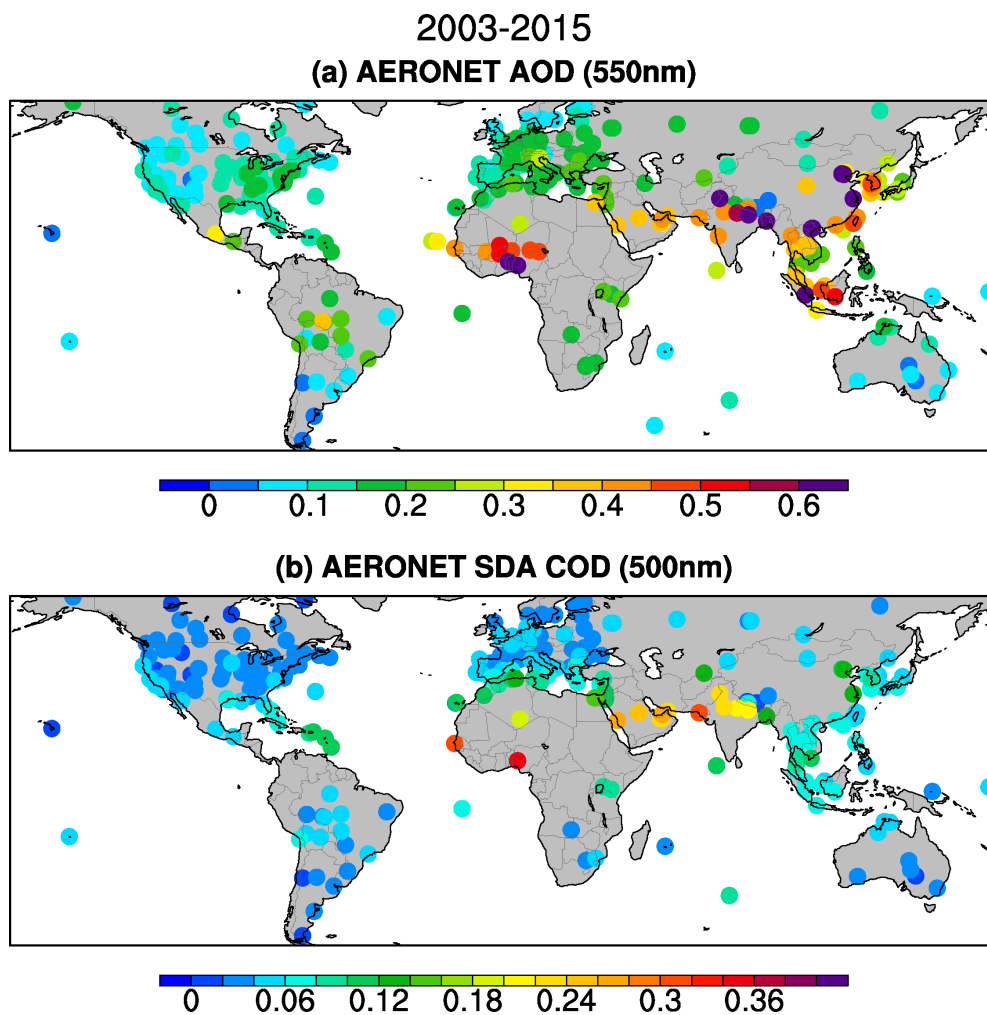
1327

1328



1329
 1330
 1331
 1332
 1333
 1334
 1335
 1336
 1337
 1338
 1339
 1340

Figure 2. (a) Cumulative frequency of $V_{\text{threshold}}$ over global land for each season (black, orange, blue, green, and grey lines denote annual, SON, JJA, MAM, and DJF averages, respectively). Color dashed lines correspond to the percentages of $V_{\text{threshold}} = 6 \text{ m s}^{-1}$ for each season and annual mean. Color arrows point to the value of $V_{\text{threshold}}$ at the 50% level in each season and annual mean. (b)-(j) distribution of annual mean $V_{\text{threshold}}$ (black bars) in each region (black boxes in Fig. 1) and for dusty seasons, i.e., MAM (green) and JJA (blue) for regions in the Northern Hemisphere and SON (orange) and DJF (grey) for regions in the Southern Hemisphere. The mean and \pm one standard deviations of $V_{\text{threshold}}$ in each region are shown on the top right of each plot.



1341

1342 Figure 3. Climatology of annual mean AERONET (a) AOD (550 nm) and (b) SDA COD
1343 (500 nm) averaged over 2003-2015.

1344

1345

1346

1347

1348

1349

1350

1351

1352

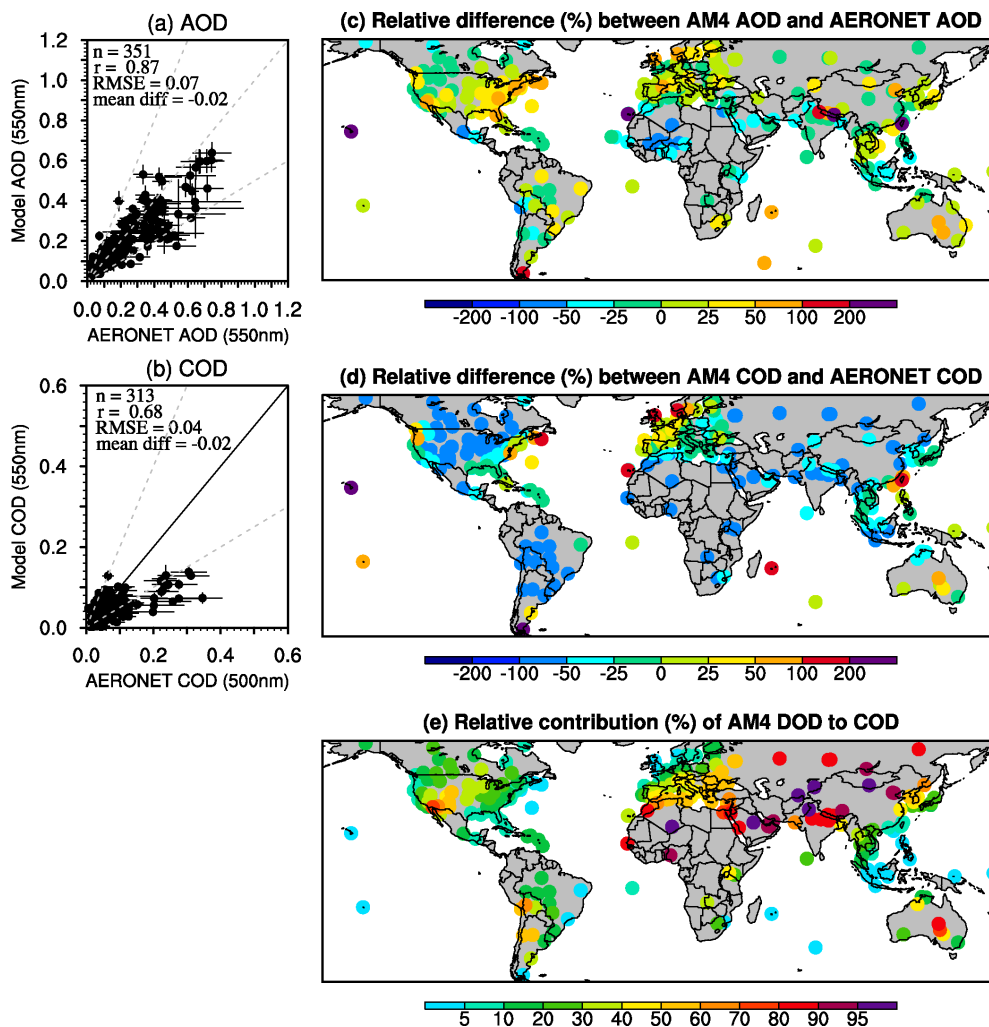
1353

1354

1355



1356



1357

1358 Figure 4. Scatter plot of simulated annual mean (a) AOD and (b) COD in the Control run
1359 versus AERONET AOD and COD (left), and the relative difference (in percentage) (c)
1360 between modeled AOD and AERONET AOD and (d) between modeled COD and
1361 AERONET COD (right). (e) The relative contribution of DOD to COD in the model.

1362

1363

1364

1365

1366

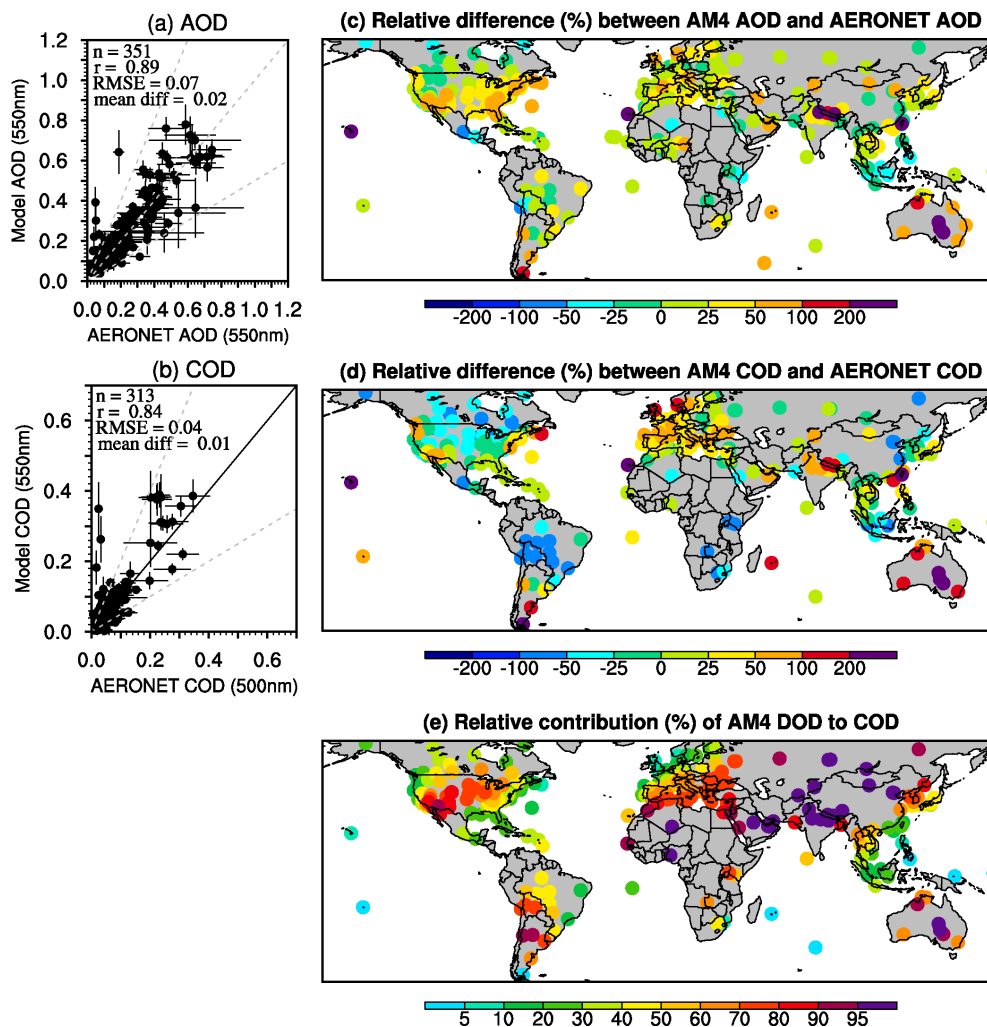
1367

1368

1369



1370



1371

1372 Figure 5. Same as Fig. 4 but for the $V_{\text{thresh}}12\text{mn}$ simulation.

1373

1374

1375

1376

1377

1378

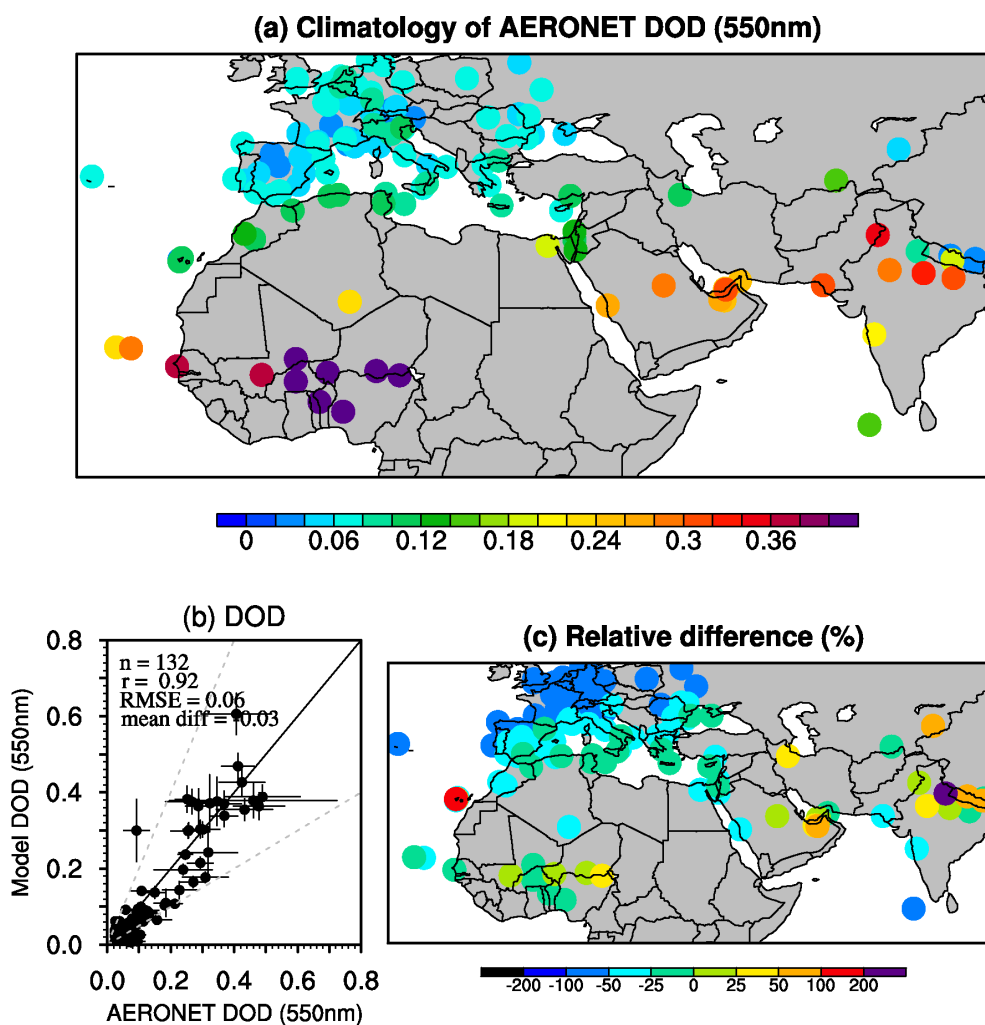
1379

1380

1381

1382

1383



1384

1385 Figure 6. (a) Climatology (2003-2015) of AERONET DOD (550 nm) over major dusty

1386 regions and (b) scatter plot of modeled DOD in the $V_{\text{thresh}}12\text{mn}$ simulation versus

1387 AERONET DOD, and (c) the relative difference (in percentage) between modeled DOD

1388 and AERONET DOD in the $V_{\text{thresh}}12\text{mn}$ simulation.

1389

1390

1391

1392

1393

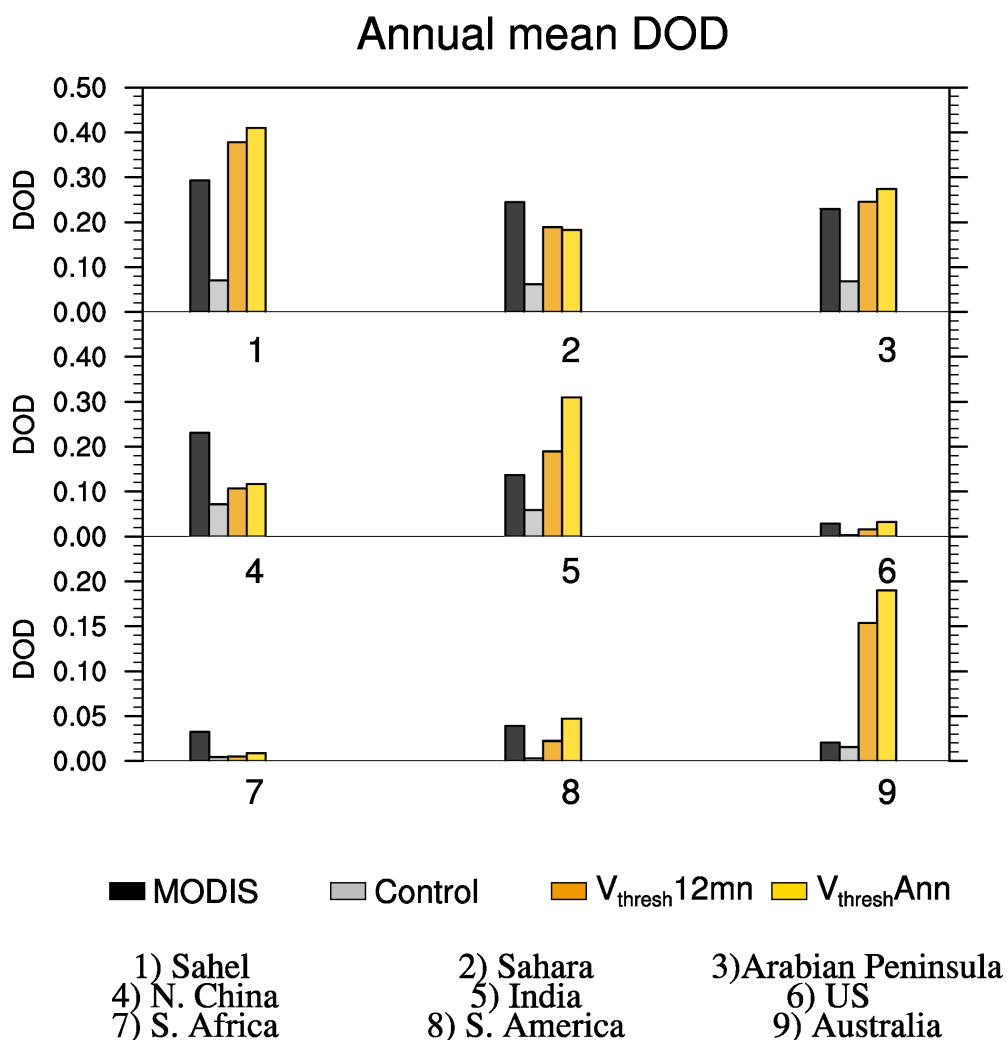
1394

1395

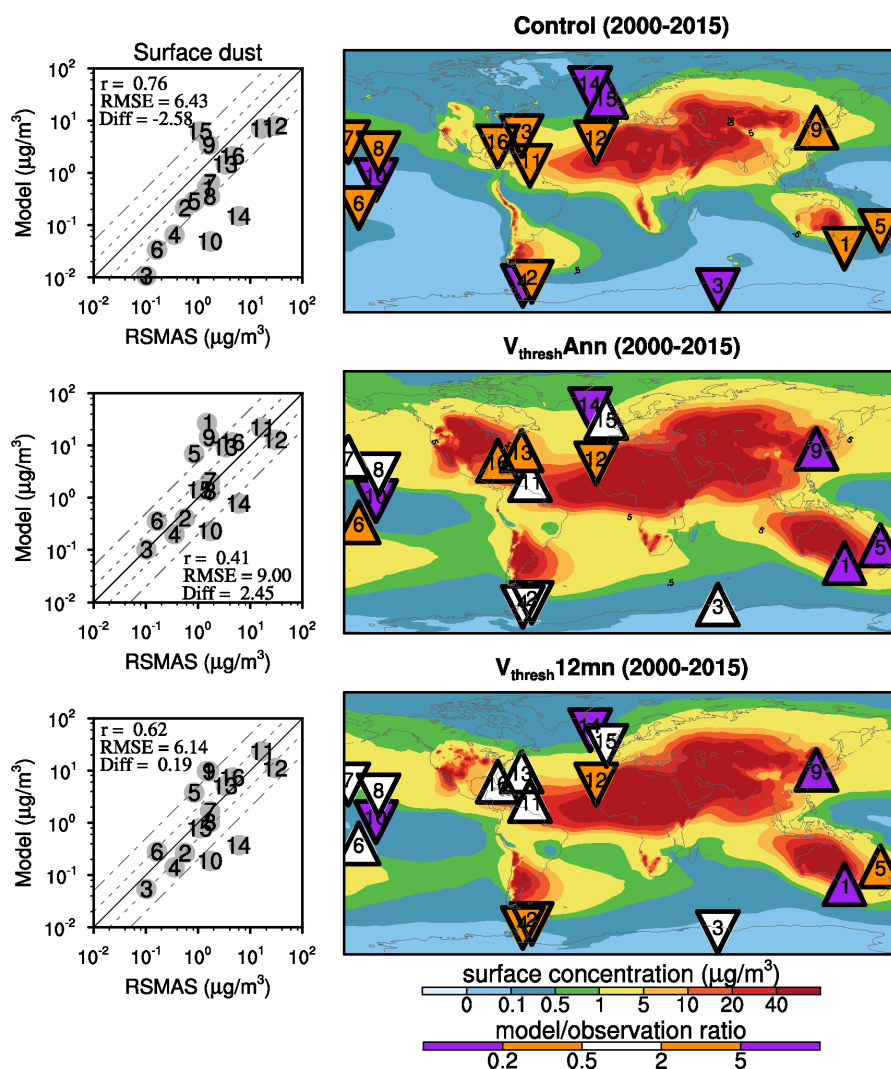
1396

1397

1398

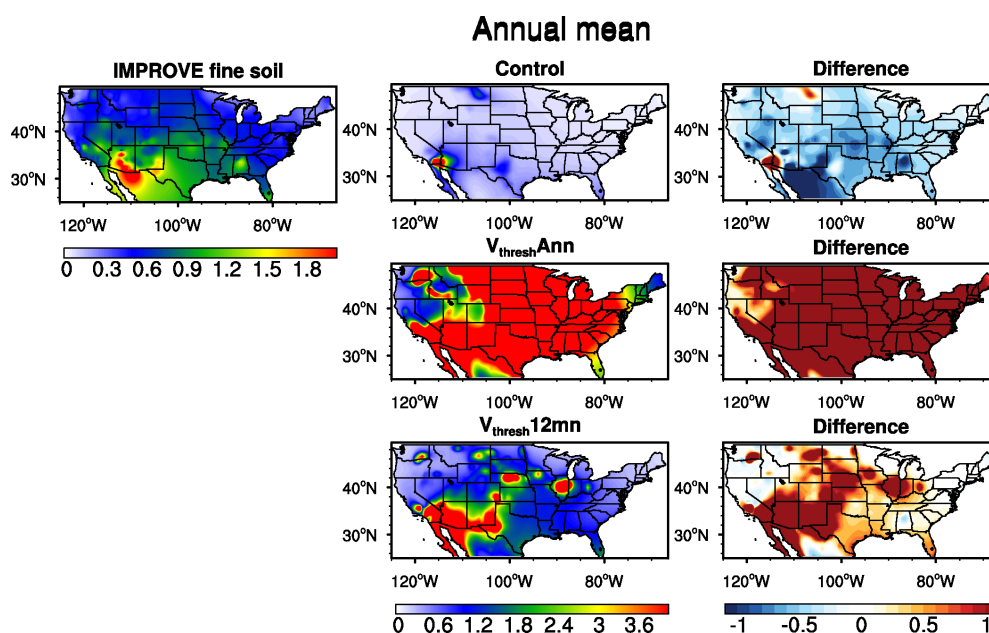


1399 Figure 7. Regional averaged annual mean DOD (2003-2015) over nine regions from the
 1400 Control (grey), $V_{\text{thresh}} 12\text{mn}$ (orange), and $V_{\text{thresh}} \text{Ann}$ (yellow) simulations and MODIS
 1401 (black).
 1402
 1403
 1404
 1405
 1406



1407
 1408
 1409
 1410
 1411
 1412
 1413
 1414
 1415
 1416
 1417
 1418

Figure 8. Scatter plots (left column) of model simulated (from top to bottom are the Control, $V_{\text{thresh Ann}}$, and $V_{\text{thresh 12mn}}$ simulations) surface dust concentration ($\mu\text{g m}^{-3}$) versus the climatology of observed surface dust concentration from RSMAS stations (Savoie and Prospero 1989), and spatial pattern of surface dust concentration from model output (shading; right column) and the ratio between modeled and RSMAS station observed surface dust concentration (color triangles, with upward triangles indicating overestimation and downward triangles indicating underestimation). 16 stations were used, and numbers in each triangle (right) and grey dots (left) indicate the stations. The one-one, one-two and one-five lines are plotted in solid, dashed and dash-dotted lines in the scatter plots.



1419

1420 Figure 9. Annual mean surface fine dust concentration ($\mu\text{g m}^{-3}$) from IMPROVE stations

1421 (left column) and three simulations (middle column) and the differences between model

1422 and observation (right column) for 2002-2015.

1423

1424

1425

1426

1427

1428

1429

1430

1431

1432

1433

1434

1435

1436

1437

1438

1439

1440

1441

1442

1443

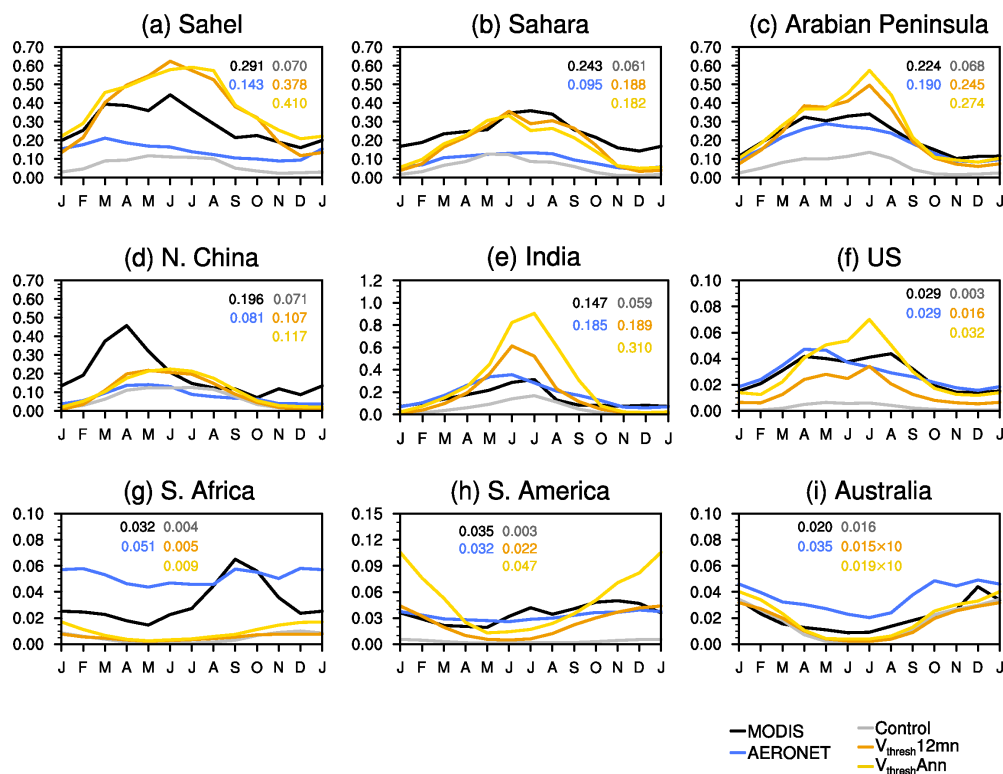
1444

1445



1446

Dust optical depth (2003-2015)



1447

1448

1449

1450

1451

1452

1453

1454

1455

1456

1457

1458

1459

1460

1461

1462

1463

1464

1465

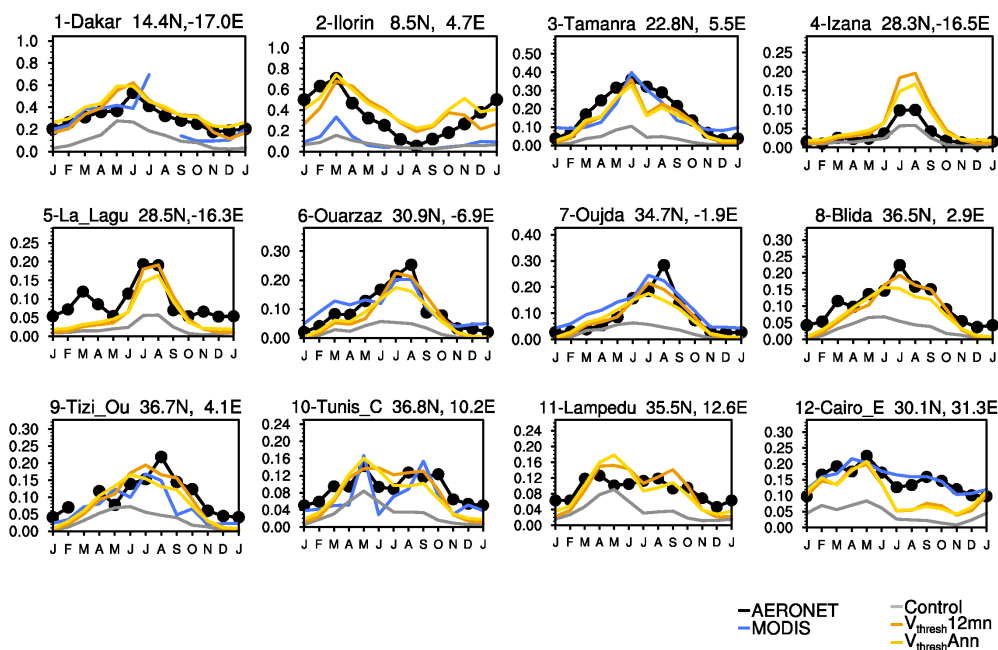
1466

Figure 10. Seasonal cycle of DOD from MODIS (black), the Control (grey), $V_{\text{thresh}12\text{mn}}$ (orange), and $V_{\text{thresh}Ann}$ (yellow) runs, and gridded AERONET SDA COD (blue) averaged over nine regions. The annual mean of each dataset in each region is listed on the top of the plot.



1467

Dust optical depth (2003-2015) N. Africa



1468

1469 Figure 11. Seasonal cycle of DOD over 12 AERONET SDA sites (see Fig. S5 in the
 1470 Supplement for locations) from the Control (grey), $V_{\text{thresh}12\text{mn}}$ (orange), and $V_{\text{thresh}Ann}$
 1471 (yellow) simulations, along with DOD from MODIS (blue), and COD from AERONET
 1472 (black dotted line). All values are averaged over 2003-2015. The location (lat/long) and
 1473 the name (due to space, only first seven characters are shown) of the sites are listed at the
 1474 top of each plot.

1475

1476

1477

1478

1479

1480

1481

1482

1483

1484

1485

1486

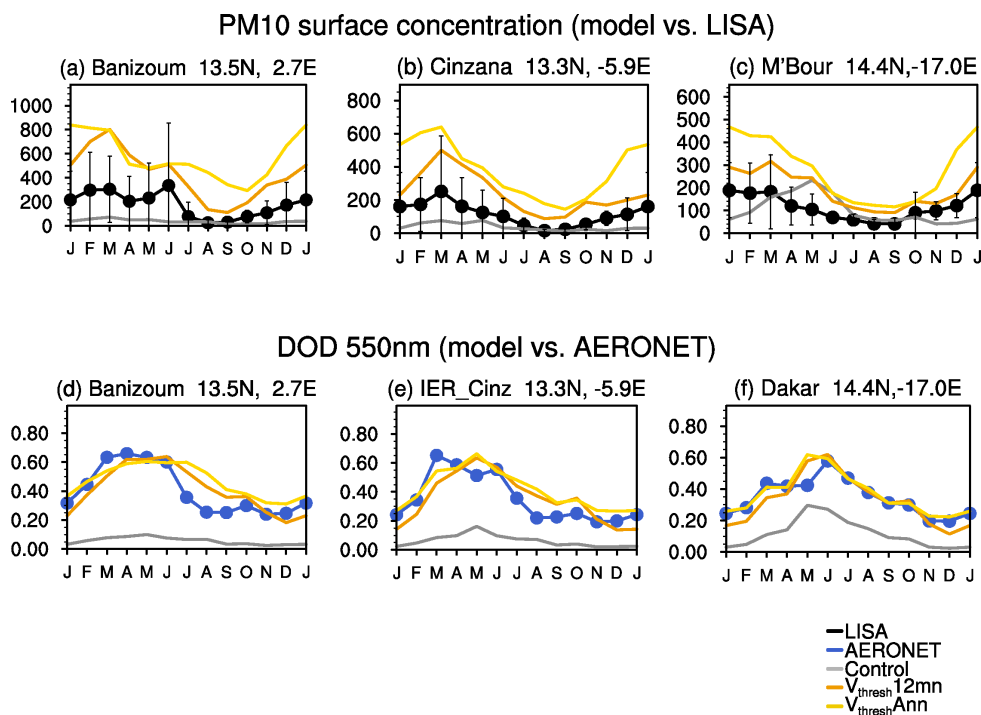
1487

1488

1489

1490

1491



1492

1493 Figure 12. (a)-(c) Seasonal cycle of PM₁₀ surface concentration (black) over three sites1494 from the LISA project, along with PM₁₀ surface dust concentration from the Control1495 (grey), $V_{\text{thresh}12\text{mn}}$ (orange), and $V_{\text{thresh}Ann}$ (yellow) simulations. Error bars are \pm one1496 standard deviations of daily mean in each month averaged over 2006-2014. Unites: $\mu\text{g m}^{-3}$.1497 ³. (d)-(f) seasonal cycle of DOD (550 nm) from three AERONET sites co-located with1498 LISA sites (blue) versus that modeled by the Control (grey), $V_{\text{thresh}12\text{mn}}$ (orange), and1499 $V_{\text{thresh}Ann}$ (yellow) simulations.

1500

1501

1502

1503

1504

1505

1506

1507

1508

1509

1510

1511

1512

1513

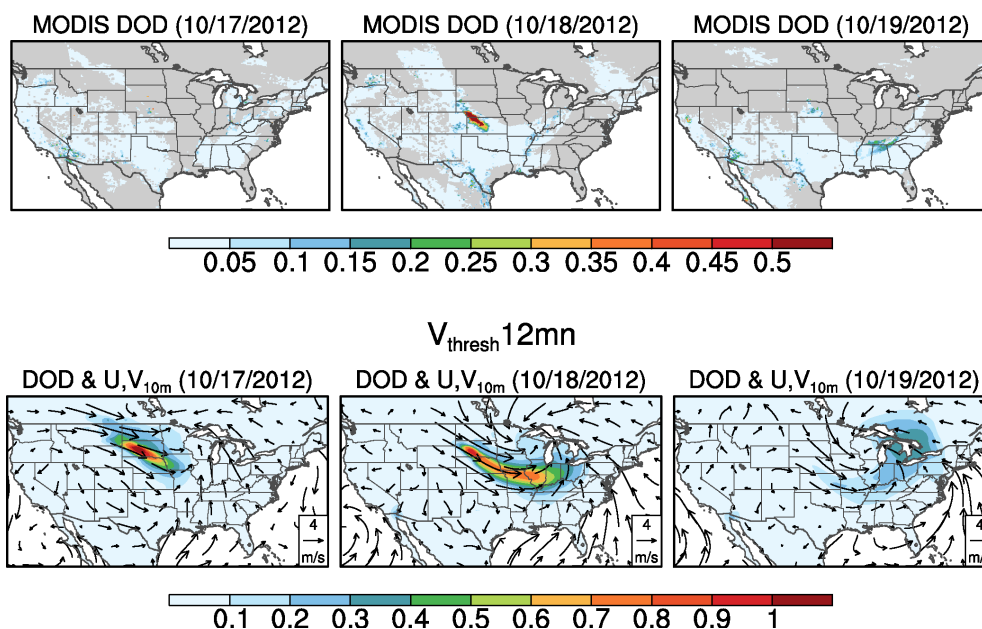
1514

1515



1516
1517
1518
1519

Case Study (Oct.17-19, 2012)

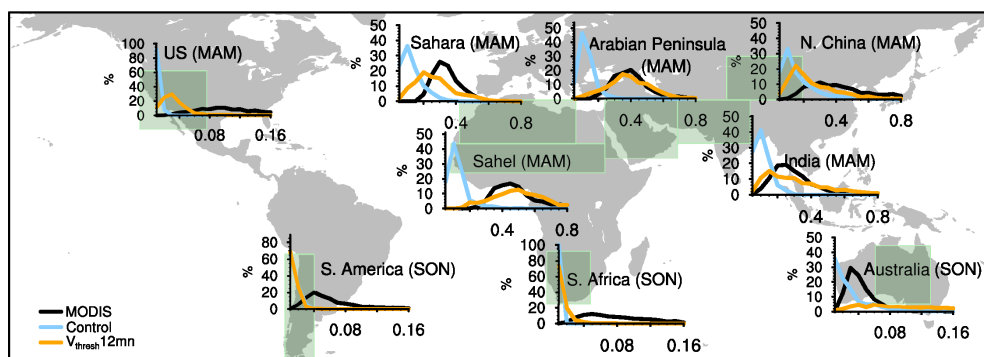


1520
1521
1522
1523
1524
1525
1526
1527
1528
1529
1530
1531
1532
1533

Figure 13. Daily DOD from MODIS (top panel), daily DOD simulated by the $V_{\text{thresh}}12\text{mn}$ run along with anomalies (with reference to the 2000-2015 mean) of surface wind vectors (m s^{-1} ; bottom panel) from Oct. 17th to Oct. 19th, 2012. Only DOD over land is shown. Missing values in MODIS DOD (top panel) are plotted in grey shading.



Frequency of DOD



1534
 1535 Figure 14. Frequency (%) distribution of regional averaged daily DOD from MODIS
 1536 (black) versus that from the Control (light blue) and $V_{\text{thresh}12\text{mn}}$ (orange) simulations for
 1537 the Sahara, the Sahel, the Arabian Peninsula, northern China, India, western to central
 1538 U.S., South America, South Africa, and Australia from 2003 to 2015. X-axis denotes the
 1539 ranges of DOD, and y-axis is percentage of occurrence. The light green boxes denote the
 1540 averaging areas. For regions in the Northern Hemisphere frequency in MAM is shown,
 1541 while for regions in the Southern Hemisphere frequency in SON is shown.

1542
 1543
 1544
 1545
 1546
 1547
 1548
 1549
 1550
 1551
 1552
 1553
 1554
 1555
 1556
 1557
 1558
 1559
 1560
 1561
 1562
 1563
 1564